



The Evolution and Origin of Ionized Gas Velocity Dispersion from $z \sim 2.6$ to $z \sim 0.6$ with KMOS^{3D}*

H. Übler¹ , R. Genzel^{1,2} , E. Wisnioski^{3,4} , N. M. Förster Schreiber¹ , T. T. Shimizu¹ , S. H. Price¹ , L. J. Tacconi¹ , S. Belli¹ , D. J. Wilman^{1,5} , M. Fossati⁶ , J. T. Mendel^{3,4} , R. L. Davies¹ , A. Beifiori^{1,5} , R. Bender^{1,5} , G. B. Brammer⁷ , A. Burkert^{1,5} , J. Chan⁸ , R. I. Davies¹ , M. Fabricius¹ , A. Galametz⁹ , R. Herrera-Camus^{1,10} , P. Lang¹¹ , D. Lutz¹ , I. G. Momcheva¹² , T. Naab¹³ , E. J. Nelson¹⁴ , R. P. Saglia^{1,5} , K. Tadaki¹⁵ , P. G. van Dokkum¹⁶ , and S. Wuyts¹⁷

¹ Max-Planck-Institut für extraterrestrische Physik, Giessenbachstr. 1, D-85748 Garching, Germany; hannah@mpe.mpg.de

² Departments of Physics and Astronomy, University of California, Berkeley, CA 94720, USA

³ Research School of Astronomy and Astrophysics, Australian National University, Canberra, ACT 2611, Australia

⁴ ARC Centre of Excellence for All Sky Astrophysics in 3 Dimensions (ASTRO 3D), Australia

⁵ Universitäts-Sternwarte Ludwig-Maximilians-Universität München, Scheinerstr. 1, D-81679 München, Germany

⁶ Institute for Computational Cosmology and Centre for Extragalactic Astronomy, Department of Physics, Durham University, South Road, Durham DH1 3LE, UK

⁷ Cosmic Dawn Center, Niels Bohr Institute, University of Copenhagen, Juliane Maries Vej 30, DK-2100 Copenhagen, Denmark

⁸ Department of Physics and Astronomy, University of California, Riverside, CA 92521, USA

⁹ Observatoire de Genève, Université de Genève, 51 Ch. des Maillettes, CH-1290 Versoix, Switzerland

¹⁰ Departamento de Astronomía, Universidad de Concepción, Avenida Esteban Iturra s/n, Casilla 160-C, Concepción, Chile

¹¹ Max-Planck-Institut für Astronomie, Königstuhl 17, D-69117 Heidelberg, Germany

¹² Space Telescope Science Institute, 3700 San Martin Drive, Baltimore, MD 21218, USA

¹³ Max-Planck-Institut für Astrophysik, Karl-Schwarzschild-Str. 1, D-85748 Garching, Germany

¹⁴ Institute for Theory and Computation, Harvard-Smithsonian Center for Astrophysics, 60 Garden Street, MS 51 Cambridge, MA 02138, USA

¹⁵ National Astronomical Observatory of Japan, 2-21-1 Osawa, Mitaka, Tokyo 181-8588, Japan

¹⁶ Department of Astronomy, Yale University, New Haven, CT 06511, USA

¹⁷ Department of Physics, University of Bath, Claverton Down, Bath, BA2 7AY, UK

Received 2019 March 28; revised 2019 May 21; accepted 2019 June 5; published 2019 July 24

Abstract

We present the $0.6 < z < 2.6$ evolution of the ionized gas velocity dispersion in 175 star-forming disk galaxies based on data from the full KMOS^{3D} integral field spectroscopic survey. In a forward-modeling Bayesian framework including instrumental effects and beam-smearing, we fit simultaneously the observed galaxy velocity and velocity dispersion along the kinematic major axis to derive the intrinsic velocity dispersion σ_0 . We find a reduction of the average intrinsic velocity dispersion of disk galaxies as a function of cosmic time, from $\sigma_0 \sim 45 \text{ km s}^{-1}$ at $z \sim 2.3$ to $\sigma_0 \sim 30 \text{ km s}^{-1}$ at $z \sim 0.9$. There is substantial intrinsic scatter ($\sigma_{\sigma_0, \text{int}} \approx 10 \text{ km s}^{-1}$) around the best-fit σ_0 - z relation beyond what can be accounted for from the typical measurement uncertainties ($\delta\sigma_0 \approx 12 \text{ km s}^{-1}$), independent of other identifiable galaxy parameters. This potentially suggests a dynamic mechanism such as minor mergers or variation in accretion being responsible for the scatter. Putting our data into the broader literature context, we find that ionized and atomic+molecular velocity dispersions evolve similarly with redshift, with the ionized gas dispersion being ~ 10 – 15 km s^{-1} higher on average. We investigate the physical driver of the on average elevated velocity dispersions at higher redshift and find that our galaxies are at most marginally Toomre-stable, suggesting that their turbulent velocities are powered by gravitational instabilities, while stellar feedback as a driver alone is insufficient. This picture is supported through comparison with a state-of-the-art analytical model of galaxy evolution.

Key words: galaxies: evolution – galaxies: high-redshift – galaxies: ISM – galaxies: kinematics and dynamics

1. Introduction

Extragalactic surveys over the last decades have produced thousands of spectrally and spatially resolved observations of galaxies from the present day out to $z \sim 4$. For massive galaxies on the star-forming main sequence, these efforts resulted in two main findings regarding their kinematic evolution: (i) already by $z \sim 2$, the majority of star-forming galaxies (SFGs) show ordered rotation, and (ii) their velocity dispersions are higher by factors of 2–5 compared to local SFGs (Labbé et al. 2003; Förster Schreiber et al. 2006, 2009, 2018; Genzel et al. 2006, 2008, 2014; Cresci et al. 2009; Epinat et al. 2009, 2012;

Law et al. 2009; Jones et al. 2010; Gnerucci et al. 2011; Wisnioski et al. 2011, 2015; E. Wisnioski et al. 2019, in preparation; Miller et al. 2012; Swinbank et al. 2012b; Stott et al. 2016; Simons et al. 2017). The redshift evolution of the ionized gas velocity dispersion has captured a lot of attention through its potential to constrain feedback and star formation models (Förster Schreiber et al. 2006; Genzel et al. 2006, 2008, 2011; Weiner et al. 2006; Kassin et al. 2007, 2012; Epinat et al. 2009, 2012; Law et al. 2009; Lehnert et al. 2009, 2013; Gnerucci et al. 2011; Wisnioski et al. 2012, 2015; Swinbank et al. 2012a; Newman et al. 2013; Simons et al. 2016, 2017; Mason et al. 2017; Turner et al. 2017; Zhou et al. 2017; Girard et al. 2018; Johnson et al. 2018).

Starting from small scales in the Milky Way, the velocity dispersion in molecular clouds is proportional to cloud size and mass, in a way that suggests molecular clouds are turbulent,

* Based on observations collected at the Very Large Telescope (VLT) of the European Southern Observatory (ESO), Paranal, Chile, under ESO program IDs 092.A-0091, 093.A-0079, 094.A-0217, 095.A-0047, 096.A-0025, 097.A-0028, 098.A-0045, 099.A-0013, 0100.A-0039, and 0101.A-0022.

with kinetic and gravitational energy being in near equipartition (Larson 1981; McKee & Ostriker 2007; Heyer & Dame 2015, and references therein). However, the lack of dependence of the turbulence level on factors such as environment or local star formation activity points toward larger scale drivers (Heyer & Brunt 2004; Brunt et al. 2009; but see Heyer & Dame 2015 for extreme environments).

In nearby galaxies, velocity dispersions of atomic gas are $\sigma_{\text{HI}} \approx 10\text{--}12 \text{ km s}^{-1}$ on scales of $\sim 100 \text{ pc}$ (Dib et al. 2006; Fukui et al. 2009; Tamburro et al. 2009; Ianjamasimanana et al. 2012; Caldú-Primo et al. 2013; Mogotsi et al. 2016; Koch et al. 2019). Molecular gas velocity dispersions are typically lower, with reported ratios in the range $\sigma_{\text{CO}}/\sigma_{\text{HI}} \approx 0.3\text{--}1$ (Fukui et al. 2009; Tamburro et al. 2009; Wong et al. 2009; Ianjamasimanana et al. 2012; Caldú-Primo et al. 2013; Druard et al. 2014; Mogotsi et al. 2016; Levy et al. 2018; Koch et al. 2019). Ionized gas velocity dispersions are substantially higher, with $\sigma_{\text{H}\alpha} \approx 24 \text{ km s}^{-1}$ (Epinat et al. 2010).

At high redshift, most measurements of gas velocity dispersion are based on ionized gas, which is accessible from the ground in the near-infrared through strong rest-frame optical lines. Typical values are $\sigma = 25\text{--}100 \text{ km s}^{-1}$ for disk galaxies. It is more challenging to measure accurate velocity dispersions at high redshift because of the combined effects of beam-smearing and limited instrumental spectral resolution (see Davies et al. 2011). The former can be corrected for instance by using the velocity field and the spatial resolution of the observations to create a beam-smearing map (e.g., Green et al. 2010; Gnerucci et al. 2011; Epinat et al. 2012), through model-based look-up tables (e.g., Burkert et al. 2016; Johnson et al. 2018), or through forward-modeling (e.g., Cresci et al. 2009; Genzel et al. 2011; Di Teodoro et al. 2016; Wuyts et al. 2016; Varidel et al. 2019). Typical spectral resolutions of near-infrared spectroscopic observations at $z \sim 1\text{--}3$ correspond to velocity dispersions of $\sigma_{\text{instrumental}} \approx 30\text{--}40 \text{ km s}^{-1}$. However, depending on the signal-to-noise ratio (S/N), it is possible to recover velocity dispersions through forward-modeling down to one-third of the instrumental resolution.

It is well established that the galactic gas velocity dispersion is correlated with redshift (e.g., review by Glazebrook 2013), but the physical processes responsible for driving and maintaining the dispersions are still debated. It has been shown theoretically that constant energy input is necessary to maintain turbulence in the interstellar medium (ISM) because it will otherwise decay within a few megayears (e.g., Mac Low et al. 1998; Stone et al. 1998). A number of potential drivers has been identified, with two main classes: (i) the conversion of kinetic energy through stellar feedback in the form of winds, expanding H II regions, and supernovae, and (ii) the release of gravitational energy through clump formation, radial flows within the disk, and accretion from the cosmic web. Other possible sources include effects of galactic rotation, fluid instabilities, and galaxy interactions (see Elmegreen & Scalo 2004 for a review). Generally, the different scales on which the proposed mechanisms operate present a challenge to simulations (see Naab & Ostriker 2017 for a review).

In this paper, we investigate the intrinsic velocity dispersion of the ionized gas phase in rotation-dominated SFGs from our KMOS^{3D} survey at $0.6 < z < 2.6$. In Section 2, we briefly present the KMOS^{3D} data set. Our modeling and sample selection is discussed in Section 3. In Section 4, we investigate the evolution of the intrinsic velocity dispersion with redshift

and put it into the broader context of multiphase literature values from $z = 4$ to $z = 0$. In Section 5, we discuss possible drivers of turbulence, particularly gravitational instabilities and stellar feedback, and compare our data to a state-of-the-art analytical model by Krumholz et al. (2018). We conclude our study in Section 6.

Throughout, we adopt a Chabrier (2003) initial mass function and a flat Λ CDM cosmology with $H_0 = 70 \text{ km s}^{-1} \text{ Mpc}^{-1}$, $\Omega_\Lambda = 0.7$, and $\Omega_m = 0.3$.

2. The KMOS^{3D} Survey

Our study is based on data from the KMOS^{3D} survey, targeting the H α line emission of primarily main-sequence galaxies in three redshift bins centered at $z \sim 0.9$, $z \sim 1.5$, and $z \sim 2.3$. The survey is presented by Wisnioski et al. (2015; E. Wisnioski et al. 2019, in preparation), to which we refer the reader for details. Below, we summarize its main characteristics.

The KMOS^{3D} galaxies were selected from the 3D-HST survey (Brammer et al. 2012; Skelton et al. 2014; Momcheva et al. 2016), providing optical-to- $8 \mu\text{m}$ photometry and, importantly, secure spectroscopic or grism redshifts, so that bright OH skylines at the location of the H α line emission could be avoided. In addition, high-resolution imaging for all galaxies is available through CANDELS (Grogin et al. 2011; Koekemoer et al. 2011; van der Wel et al. 2012) and further multiwavelength coverage through photometry from *Spitzer*/MIPS and *Herschel*/PACS (Lutz et al. 2011; Magnelli et al. 2013; Whitaker et al. 2014, and references therein).

For the KMOS^{3D} survey, we selected galaxies with stellar masses $\log(M_*/M_\odot) > 9$ and $K_{\text{AB}} \lesssim 23$. The selection aimed to provide a homogeneous coverage of the star formation main sequence across stellar mass in the three redshift slices, thus ensuring near equal statistical coverage up to the highest masses. In addition, KMOS^{3D} also extends below the main-sequence regime where galaxies are “quiescent,” and it contains starburst outliers above the main sequence.

Stellar masses were derived following Wuyts et al. (2011) by fitting the broad- and medium-band optical-to-mid-infrared spectral energy distribution with Bruzual & Charlot (2003) stellar population synthesis models, adopting a Calzetti et al. (2000) extinction law, solar metallicity, and a range of star formation histories. Gas mass measurements are not available for most of our galaxies. We exploit the scaling relation by Tacconi et al. (2018), which depends on redshift, offset from the main sequence, and stellar mass, with the main-sequence prescription by Whitaker et al. (2014), to estimate the molecular gas masses (M_{gas}) of our galaxies. We do not account for atomic gas in this study. The derivation of star formation rates (SFRs) followed the ladder of SFR indicators as described by Wuyts et al. (2011).

Structural properties such as the axis ratio $q = b/a$, the disk effective radius R_e , and the bulge-to-total stellar mass fraction B/T are based on two-dimensional Sérsic models to the stellar light distribution high-resolution *H*-band images from *Hubble Space Telescope* (*HST*) observations (van der Wel et al. 2012; Lang et al. 2014). For the effective radius, we apply a color correction following van der Wel et al. (2014b).

The survey was conducted during the years 2013–2018 with the multiplexing near-infrared integral field spectrograph KMOS (Sharples et al. 2004, 2013) at the Very Large Telescope (VLT).

The full KMOS^{3D} sample consists of 740 targeted galaxies (E. Wisnioski et al. 2019, in preparation).

3. Dynamical Modeling and Sample Selection

We constrain the intrinsic velocity dispersions by forward-modeling the observed one-dimensional velocity and velocity dispersion profiles extracted from the data cubes. For this work, we use the two-dimensional kinematic information to determine the kinematic major axis and to distinguish rotation-dominated, dispersion-dominated, and disturbed systems. The full kinematic information on the motions of stars or gas in the plane of a rotating disk can be extracted along its kinematic major axis. Modeling the one-dimensional kinematics instead of the two- or three-dimensional data increases the S/N of our measurements and thus allows us to study a larger sample of galaxies with reliable modeling. We have verified that this has only a minor impact on the derived dynamical parameters, with an average, nonsystematic difference of one-dimensional versus two-dimensional intrinsic velocity dispersion of $\sim 5\%$ – 10% .

3.1. One-dimensional Kinematic Profiles

We derive two-dimensional projected H α velocity and velocity dispersion fields for all KMOS^{3D} galaxies using LINEFIT (Davies et al. 2009, 2011; Förster Schreiber et al. 2009), a code that takes into account the instrument line-spread function and fits a Gaussian model for each spaxel of the reduced data cube after continuum subtraction. From these maps, we exclude spaxels with $S/N \leq 2$, uncertainties on the velocity or velocity dispersion of $\geq 100 \text{ km s}^{-1}$, as well as off-source fits to noise features. We determine the maximum and minimum of the velocity map through a weighted average of either the 5% of spaxels of both the highest and lowest velocity values for galaxies with ≥ 50 suitable spaxels, or otherwise of the five spaxels with highest and lowest velocities. The kinematic major axis is defined as the line going through the maximum and minimum of the velocity map. The kinematic center is defined as the midpoint on the kinematics major axis connecting the maximum and minimum of the velocity map. This method follows the procedures outlined by Wisnioski et al. (2015), and in the KMOS^{3D} data release and final survey paper by E. Wisnioski et al. (2019, in preparation).

Along the kinematic major axis, we then extract spectra in circular apertures of diameter $2 \times \text{FWHM}$ of the model-independent point-spread function (PSF) associated with each individual galaxy. Here, the flux from all spaxels within an aperture is integrated to create a single spectrum. For the dynamical modeling of our galaxies (see Section 3.2), we repeat this same procedure for each iteration of the model fitting to properly account for any effects related to this integration process. We consider a galaxy to be spatially resolved if we can measure its kinematics over a total of at least $3 \times \text{PSF}_{\text{FWHM}}$ along the kinematic major axis. We fit the H α velocity and velocity dispersion from the resulting spectra, providing us with the one-dimensional rotation curve $v_{\text{rot}}(r) \cdot \sin(i)$ and dispersion profile $\sigma(r)$, uncorrected for beam-smearing. Uncertainties for each data point are derived using Monte Carlo analysis and have typical values of 6 km s^{-1} and 10 km s^{-1} for the velocity and dispersion values, respectively.

With this methodology, we have successfully extracted kinematic profiles for all 535 KMOS^{3D} H α -detected galaxies with secure redshifts.

3.2. Dynamical Modeling with DYSMAL

As a next step, we consider all galaxies with kinematic profile extractions that are resolved—a total of 456 SFGs. We further exclude targets for which we detect multiple systems within the IFU, and we eliminate merging or potentially interacting systems with larger separations based on projected distances, redshift separations, and mass ratios, as informed through the 3D-HST catalog (J. T. Mendel et al. 2019, in preparation). Galaxies that are strongly contaminated by sky features, have prominent broad-line regions, or have very strong outflows affecting the recovery of the galaxies' velocity and dispersion are also excluded. This results in 356 galaxies.

We exploit the dynamical fitting code DYSMAL (Cresci et al. 2009; Davies et al. 2011; Wuyts et al. 2016; Übler et al. 2018) to model our galaxies. DYSMAL is a forward-modeling code that allows for a flexible number of components (disk, bulge, halo, etc.) and free parameters. It accounts consistently for finite scale heights and flattened spheroidal potentials (Noor-dermeer 2008), and it includes the effects of pressure support on the rotation velocity. It also accounts for the instrument line-spread function and for beam-smearing effects by convolving with the two-dimensional PSF of each galaxy.

For our modeling, we assume a velocity dispersion that is isotropic and constant throughout the disk, motivated by deep adaptive optics imaging spectroscopy on kiloparsec scales of 35 $z = 1$ – 2.6 SFGs in the SINS/zC-SINF sample (Genzel et al. 2006, 2008, 2011, 2017; Cresci et al. 2009; Förster Schreiber et al. 2018; see also Section 5.2). We note that for nearby galaxies, radially declining velocity dispersions have been observed for atomic and molecular gas (van der Kruit & Freeman 1984; Dickey et al. 1990; Boulanger & Viallefond 1992; Kamphuis & Sancisi 1993; Meurer et al. 1996; Petric & Rupen 2007; Tamburro et al. 2009; Wilson et al. 2011; Caldú-Primo et al. 2013; Mogotsi et al. 2016; Sun et al. 2018; Koch et al. 2019), where the velocity dispersion usually reaches a constant level only in the disk outskirts. The observed radial changes in velocity dispersion are, however, rarely larger than 10 – 20 km s^{-1} , and such variations on small scales are likely washed out through the coarser spatial resolution of typical high- z observations (but see Section 5.2 for a high-resolution example).

We create a three-dimensional mass model of each galaxy consisting of an exponential disk with the effective radius R_e adopted from the H -band measurements, with the ratio of scale height to scale length $q_0 = 0.25$, and with a central bulge ($R_{e,\text{bulge}} = 1 \text{ kpc}$, Sérsic index $n_{\text{S,bulge}} = 4$; e.g., Lang et al. 2014; Tacchella et al. 2015b). The value of $q_0 = 0.25$ is motivated by the falloff in the $q = b/a$ distribution of SFGs at the mass and redshift of our sample (van der Wel et al. 2014a). For galaxies without an H -band-based measurement of the bulge mass (see Section 2; ca. 30%), we use average values of $B/T = [0.25; 0.35; 0.45; 0.5]$ for total stellar masses of $\log(M_*/M_\odot) = [<10.8; 10.8$ – $11; 11$ – $11.4; >11.4]$, following Lang et al. (2014). We fix the physical size of the bulge because individual measurements of $R_{e,\text{bulge}}$ are very uncertain, in contrast to measurements of B/T (see Tacchella et al. 2015b). In a population-averaged sense, however, $R_{e,\text{bulge}} = 1 \text{ kpc}$ is a robust choice (see Lang et al. 2014). We calculate the galaxy inclination i as $\cos(i) = [(q^2 - q_0^2)/(1 - q_0^2)]^{1/2}$. The mass

model is then rotated to match the galaxy’s observed orientation in space, convolved with the line-spread function and the PSF of the observation to take into account beam-smearing, and subsequently pixelated to resemble the spatial sampling of the observation. We approximate the PSF as a two-dimensional Moffat function that has been fitted to the standard star observations associated with each KMOS detector and pointing. For our modeling, we assume that light traces mass.

Using DYSMAL, we simultaneously fit the one-dimensional velocity and velocity dispersion profiles of our galaxies in observed space. The best-fitting intrinsic rotation velocity, v_{rot} , is constrained both through the mass model and the intrinsic velocity dispersion via pressure support. We apply Markov Chain Monte Carlo (MCMC) sampling to determine the model likelihood based on comparison to the observed one-dimensional kinematic profiles and assuming Gaussian measurement noise. To ensure convergence of the MCMC chains, we model each galaxy with 400 walkers, a burn-in phase of 50–100 steps, followed by a running phase of another 50–100 steps (>10 times the maximum autocorrelation time of the individual parameters). For each free parameter, we adopt the median of all model realizations as our best-fit value, with asymmetric uncertainties corresponding to the 1σ confidence ranges of the one-dimensional marginalized posterior distributions.

In order to recover the intrinsic velocity dispersion as best as possible, we consider a total of three setups with varying free parameters and treatment of the kinematic profiles:

1. In our first setup, we feed the kinematic profiles obtained as described in Section 3.1, with free parameters being the total dynamical mass in the range $\log(M_{\text{tot}}/M_{\odot}) = [9; 13]$, and the intrinsic velocity dispersion in the range $\sigma_0 = [5; 300] \text{ km s}^{-1}$. M_{tot} is the total mass distributed in the three-dimensional disk plus bulge structure necessary to reproduce the observed kinematics. Other parameters are fixed, specifically i , R_e , and B/T .
2. Due to extinction, skyline contamination, and noise limitations, some galaxies display asymmetric kinematic profiles. Therefore, we employ a symmetrization technique in a second setup, where the one-dimensional profiles are folded (for the dispersion profile) or rotated (for the rotation curve) around the kinematic center, interpolated onto a common grid, and averaged by calculating the mean at each radial grid point to obtain symmetric profiles, with uncertainties added in quadrature. Again, the free parameters are M_{tot} and σ_0 , allowed to vary within the same ranges as for setup 1.
3. As noted in Section 2, the R_e and B/T of our galaxies are derived from H -band imaging. It is known that the mass distribution derived from the H -band light might differ from the corresponding $H\alpha$ flux profiles (e.g., Wuyts et al. 2012; Tacchella et al. 2015a; Nelson et al. 2016; D. J. Wilman et al. 2019, in preparation). In particular, the dispersion profiles can be sensitive to the central mass concentration. In the third setup, we therefore proceed as in setup 2, but additionally leave the disk effective radius R_e and the bulge-to-total fraction B/T as free parameters. For R_e , we use an effectively flat prior centered on the fiducial value, and truncated at ± 2.5 kpc, with hard bounds of $R_e = [0.1; 20] \text{ kpc}$. For B/T , we use an effectively flat prior with hard bounds of $B/T = [0; 1]$.

Table 1

Comparison of Modeling Results from the Three Setups (S1, S2, S3) Described in Section 3.2

Comparison	Quantity	Mean	Std. Dev.
S1–S2	$\Delta\sigma_0$ (km s ^{−1})	0.9	6.0
	$\Delta\log(M_{\text{tot}})$ (dex of M_{\odot})	−0.01	0.03
S1–S3	$\Delta\sigma_0$ (km s ^{−1})	0.5	7.4
	$\Delta\log(M_{\text{tot}})$ (dex of M_{\odot})	−0.06	0.11
S2–S3	$\Delta\sigma_0$ (km s ^{−1})	−1.4	5.3
	$\Delta\log(M_{\text{tot}})$ (dex of M_{\odot})	−0.04	0.10
S3: H -band– $H\alpha$ ^a	ΔR_e (kpc)	−0.6	1.0
	$\Delta B/T$	0.03	0.14

Note.

^a Comparison of the fiducial R_e and B/T as derived from the stellar light H -band images (see Section 2) to the modeling results from setup 3, where we fit for R_e and B/T as detailed in Section 3.2.

Comparing results from the three setups, we generally find good agreement for both the derived intrinsic dispersions and the dynamical masses, as listed in Table 1. For setup 3, the model-derived (mass/ $H\alpha$) effective radii are systematically higher compared to the H -band measurements by ~ 0.6 kpc. For the range of $R_e \approx 2$ –10 kpc and $\log(M_{*}/M_{\odot}) \approx 9.2$ –11.5 in our kinematic sample, this is in agreement with the results by Nelson et al. (2016) and D. J. Wilman et al. (2019, in preparation), who find $R_{e,H\alpha}/R_{e,H} \approx 1.1$ –1.2 from high-resolution HST observations and from our full KMOS^{3D} sample, respectively. The average agreement between the H -band-derived B/T and the model-derived B/T is better; however, the model-derived value is likely more realistic for cases with only a grid-based B/T .

We tested a fourth setup for a subset of our sample, including not only the bulge and disk components but in addition an NFW halo (Navarro et al. 1996), with a prior on the expected dark matter halo mass (Moster et al. 2018) and the concentration parameter fixed to the theoretically expected value (Dutton & Macciò 2014). The resulting best-fit velocity dispersions are robust in that they agree within the uncertainties with the results from the other three setups with a standard deviation of 5.9 km s^{-1} , and there are no systematic effects. However, the limited field-of-view of KMOS (compared to e.g., SINFONI) together with our typical integration times of 5–9 hr per target constrain our ability to map the faint outskirts of galaxies where the kinematics are most sensitive to additional dynamical components with a different mass distribution. Therefore, we do not include fits from this fourth setup in our final sample.

3.3. The Kinematic Sample

We inspect the fits from all three model setups to create our best-fit sample. By default, we choose the fit to setup 1, but if it is bad or poorly constrained, we consider setups 2 and 3 in this order. Galaxies with poor fits in all setups are excluded. With this strategy, we stay as closely as possible to the original data, but at the same time do not need to disregard galaxies with one-sided extinction or skyline contamination that otherwise show good data quality, and we can choose fits from setup 3 with a more appropriate mass distribution, if necessary.

Finally, we impose a $v_{\text{rot}}/\sigma_0 \geq 1$ cut to focus on rotation-dominated systems. Here, v_{rot} is the model intrinsic rotation

velocity at $1.38 R_e$, which is the location of the peak of the rotation curve for a Noordermeer disk with $n_s = 1$. Our final sample consists of 175 galaxies, with 80, 47, and 48 galaxies in the redshift slices $z = 0.6\text{--}1.1$, $z = 1.2\text{--}1.7$, and $z = 1.9\text{--}2.6$. Of those galaxies, 56% are from setup 1, 31% from setup 2, and 13% from setup 3. We show examples of galaxies and their fits from different setups in Appendix A. The averaged uncertainties on our derived σ_0 values cover the range $\delta\sigma_0 = 2\text{--}29 \text{ km s}^{-1}$, with 68th percentiles of $\delta\sigma_0 = 5\text{--}15 \text{ km s}^{-1}$, and mean values in the three redshift slices $z \sim 0.9, 1.5$, and 2.3 of $\delta\sigma_0 = 8, 10$, and 13 km s^{-1} . Asymmetric uncertainties can be as high as $\delta\sigma_0 = 37 \text{ km s}^{-1}$.

In Figure 1, we compare physical properties of our final sample (blue shading) to the underlying representative population of SFGs from the 3D-HST survey (gray shading) and to the full KMOS^{3D} sample (pink lines). Compared to our full KMOS^{3D} sample, we have not selected preferentially in redshift. In terms of stellar mass, both our full KMOS^{3D} sample and our kinematic sample include fewer lower mass systems compared to the 3D-HST galaxies, such that our sample is not mass-complete. This is mainly a consequence of the $K_{AB} \lesssim 23$ cut. With respect to the main sequence of SFGs, however, our kinematic sample follows the distribution of both the full KMOS^{3D} and the 3D-HST sample. The fraction of systems with effective radii below the population average is smaller for our kinematic sample compared to the 3D-HST and KMOS^{3D} samples. This is due to our conservative definition of resolved kinematics, where we request measurements over at least $3 \times \text{PSF}_{\text{FWHM}}$, with the primary effect of reducing the number of galaxies with $R_e < 2$ kpc. Generally, for very small systems, it is more challenging to recover the intrinsic velocity dispersion, because the kinematics are often unresolved (but see Wisnioski et al. 2018 for a detailed study of the kinematics of compact galaxies in the KMOS^{3D} survey). Axis ratios of our galaxies are homogeneously distributed, following the KMOS^{3D} and 3D-HST parent samples (see also Section 3.6).

In Figure 2, we show SFR (top) and size (bottom) both as a function of stellar mass for the 3D-HST parent sample (gray density histogram), the full KMOS^{3D} sample (purple diamonds), and our final kinematic sample at redshifts $z \sim 0.9$ (blue circles), $z \sim 1.5$ (green pentagons), and $z \sim 2.3$ (red hexagons). The figure illustrates the homogeneous coverage of the KMOS^{3D} survey of typical main-sequence galaxies over more than two orders of magnitude in stellar mass. Similarly, the galaxies from our final sample are distributed along the main sequence and have typical sizes for their redshifts, with a tendency toward higher-than-average sizes particularly at $z \sim 2.3$. This bias at the highest redshifts is introduced through our conservative definition of resolved galaxies and ensures robust σ_0 measurements even at these high redshifts.

3.4. Upper Limit Cases

Our final sample contains 28 galaxies for which the best-fit σ_0 value within the 1σ uncertainties is lower than 10 km s^{-1} . In using the $H\alpha$ line, we are supposedly tracing emission originating from ionized H II regions. Due to thermal broadening ($\sigma_{\text{th}} \approx 10 \text{ km s}^{-1}$) as well as the expansion of H II regions ($v_{\text{ex}} \gtrsim 10 \text{ km s}^{-1}$), we expect some minimum velocity dispersion for the average galaxy of $\sigma_0 \approx 10\text{--}15 \text{ km s}^{-1}$ (Shields 1990).

This minimum value is lower than the typical spectral resolution of KMOS: the effective FWHM spectral resolution

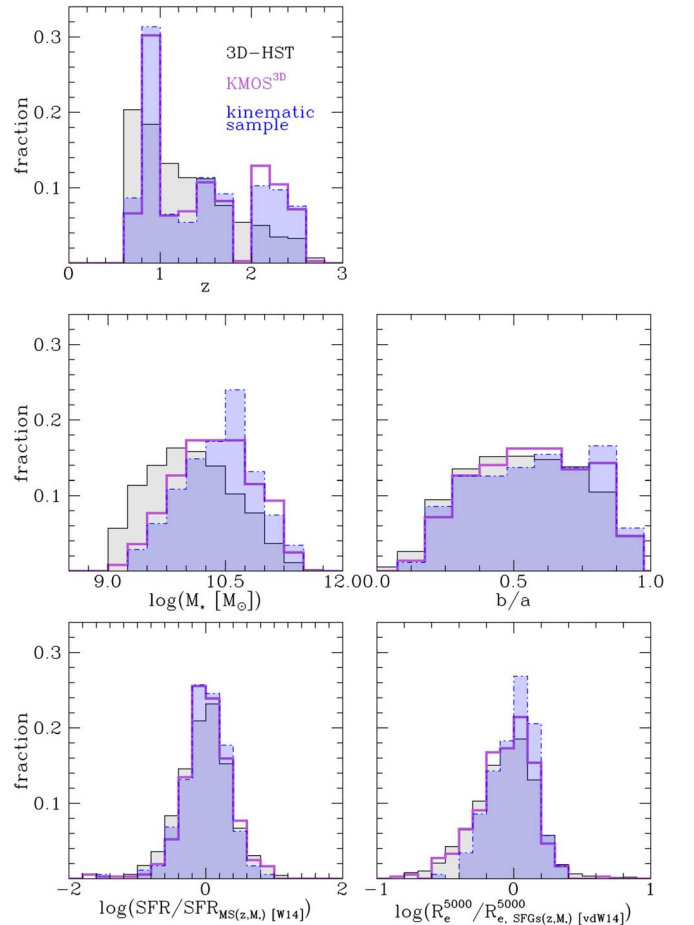


Figure 1. Distribution of physical properties of our kinematic sample (blue shading) compared to the full KMOS^{3D} survey (pink lines) and the underlying star-forming galaxy population at $0.6 < z < 2.7$ taken from the 3D-HST source catalog (gray shading) with $\log(M_*/M_\odot) \geq 9$, $K_{AB} < 23$ mag, and $\text{SFR}/M_* > 0.7/t_{\text{Hubble}}$. We show the redshift z (top left), stellar mass (middle left), axis ratio b/a (middle right), offset from the main sequence (bottom left), and offset from the mass–size relation (bottom right). The SFR is normalized to the main sequence as derived by Whitaker et al. (2014) at the redshift and stellar mass of each galaxy, using the redshift-interpolated parameterization by Wisnioski et al. (2015). The effective radii as measured from the H band are corrected to the rest-frame 5000 \AA and normalized to the mass–size relation of SFGs as derived by van der Wel et al. (2014b) at the redshift and stellar mass of each galaxy. For our kinematic sample, there is no selection bias in redshift z , axis ratio b/a , or offset from the main sequence. Due to the $K_{AB} < 23$ mag cut for our KMOS^{3D} survey, KMOS^{3D} galaxies have higher stellar masses compared to the 3D-HST sample. Galaxies in our kinematic sample have on average larger sizes compared to all KMOS^{3D} galaxies as well as the 3D-HST sample. This is due to our conservative definition of resolved kinematics (see Section 3.1).

at the $H\alpha$ line measured from the reduced data of galaxies in our KMOS^{3D} survey is $\Delta R = \lambda/\Delta\lambda \sim 3515, 3975$, and 3860 in the YJ, H , and K bands, respectively (E. Wisnioski et al. 2019, in preparation). For our kinematic sample, the corresponding mean spectral resolutions are $\sigma_{\text{instrumental}} \sim 37, 32$, and 34 km s^{-1} . However, as discussed in more detail in E. Wisnioski et al. (2019, in preparation), within the bands there are variations of the spectral resolution of up to $\Delta R = 1000$ for individual IFUs. It is therefore crucial to measure the associated spectral resolution at $H\alpha$ for each individual galaxy from sky or arc lines in order to reliably recover the velocity dispersion, as it is done for KMOS^{3D}.

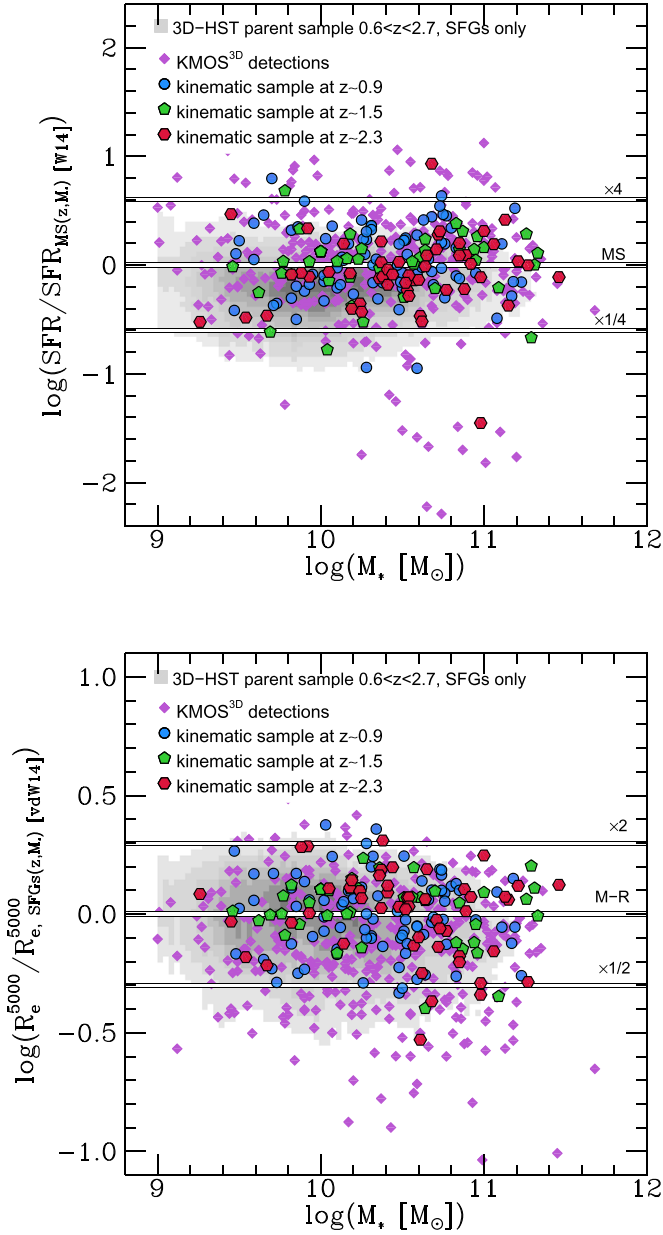


Figure 2. Location of our kinematic sample in the M_* –SFR (top) and M_* – R_e (bottom) planes compared to all detected KMOS^{3D} galaxies (pink diamonds) and the underlying star-forming galaxy population at $0.6 < z < 2.7$ taken from the 3D-HST source catalog (gray scale) with $\log(M_*/M_\odot) \geq 9$, $K_{AB} < 23$ mag, and $\text{SFR}/M_* > 0.7/t_{\text{Hubble}}$. In the top panel, the SFR is normalized to the main sequence as derived by Whitaker et al. (2014) at the redshift and stellar mass of each galaxy, using the redshift-interpolated parameterization by Wisnioski et al. (2015). In the bottom panel, the effective radii as measured from the H band are corrected to the rest-frame 5000 Å and normalized to the mass–size relation of SFGs derived by van der Wel et al. (2014b) at the redshift and stellar mass of each galaxy. The galaxies in our kinematic sample are distributed along the main sequence and have typical sizes for their redshifts. However, the size distribution of our targets is biased toward higher-than-average sizes, also compared to our KMOS^{3D} parent sample. This is introduced by selecting only galaxies with resolved kinematics (see Section 3.1).

Our line-fitting procedure can recover intrinsic velocity dispersions that are a fraction of the instrumental resolution. However, these measurements get increasingly uncertain for decreasing intrinsic velocity dispersions. For galaxies for which the best-fit σ_0 value within the 1σ uncertainties is lower than 10 km s^{-1} , we adopt as a conservative upper limit the upper 2σ

Table 2
Spearman Rank Correlation Coefficients, ρ_s , and Their Significance σ_ρ , between σ_0 and, Respectively, R_e , R_{max}/R_e , $\sigma_{\text{instrumental}}$, and b/a

Quantity	ρ_s	σ_ρ
R_e	0.01	1.2
R_{max}/R_e	−0.05	0.7
$\sigma_{\text{instrumental}}$	−0.07	0.9
b/a	−0.04	0.5

boundary of the marginalized posterior distribution derived from the MCMC chain. The resulting upper limits lie between 18 and 53 km s^{-1} .

3.5. Validation of PSF and Line-spread Function Corrections

Before we investigate in detail the redshift evolution of σ_0 and its potential drivers, we want to exclude any residual effects of beam-smearing. Therefore, we consider σ_0 as a function of the effective radius, R_e , and of the ratio of the outermost measured data point to the effective radius, R_{max}/R_e .

We do not find significant correlations with R_e or R_{max}/R_e , as listed in Table 2 (for R_e see also Figure 16). We would expect correlations with these parameters if unresolved rotation enters our measure of the velocity dispersion. As mentioned in Sections 3.1 and 3.3, we only consider galaxies for our final sample for which we can extract kinematics over a distance of at least $3 \times \text{PSF}_{\text{FWHM}}$, with a mean value of $4 \times \text{PSF}_{\text{FWHM}}$. However, the extracted kinematics can still be affected by beam-smearing even in the outer parts of the galaxies. The fact that we do not find correlations with size implies that our forward-modeling procedure properly accounts for beam-smearing even for the smaller systems we include.

Similarly, we test for correlations of σ_0 with instrumental resolution and again we do not find a significant correlation, indicating that both our kinematic fitting code and forward-modeling procedure properly account for the instrumental line-spread function (see Table 2).

3.6. Vertical versus Radial Velocity Dispersion

For local galaxies, there exists a correlation between galaxy inclination and line-of-sight velocity dispersion. This is due to the transition from measuring predominantly vertical velocity dispersion in face-on systems to measuring predominantly radial velocity dispersion in edge-on systems, with a typical ratio of $\sigma_z/\sigma_r \sim 0.6$ (van der Kruit & Freeman 2011; Glazebrook 2013). For instance, Leroy et al. (2008) find for the THINGS sample that the HI line-of-sight velocity dispersion increases for galaxies with $i > 60^\circ$ ($b/a < 0.5$), as does the variation of velocity dispersion in individual galaxies. Intriguingly, evidence for higher velocity dispersions in more edge-on systems has been found in the higher resolution $z \sim 1$ –2 data from the SINS survey (Genzel et al. 2011). For our KMOS^{3D} kinematic sample, and in agreement with the earlier results by Wisnioski et al. (2015), we do not find a correlation between σ_0 and b/a , as shown in Figure 3 and Table 2, possibly due to the coarser spatial resolution of our data.

4. Velocity Dispersion Increases with Redshift

Previous studies have shown that the velocity dispersion of SFGs increases with redshift (Förster Schreiber et al. 2006; Genzel et al. 2006, 2011; Weiner et al. 2006; Kassim et al.

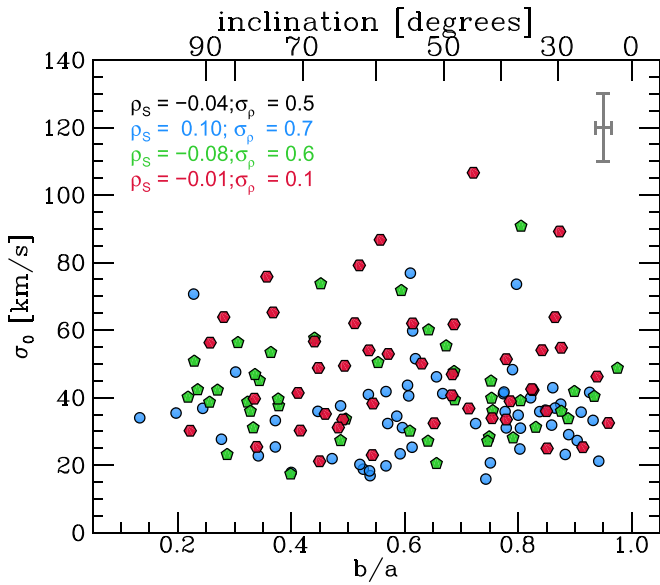


Figure 3. Intrinsic velocity dispersion σ_0 as a function of axis ratio b/a as measured from the H band. Spearman rank correlation coefficients ρ_s and their significance σ_p are given in the panel for the full sample (black) and their redshift slices at $z \sim 0.9$ (blue), $z \sim 1.5$ (green), and $z \sim 2.3$ (red). A typical error bar is shown in the top-right corner. We do not find significant correlations between σ_0 and b/a for the full sample nor the individual redshift bins.

2007, 2012; Wisnioski et al. 2012, 2015; Newman et al. 2013; Simons et al. 2016, 2017; Mason et al. 2017; Turner et al. 2017; Johnson et al. 2018), albeit with large uncertainties and scatter. In the following, we confirm and increase the robustness of this conclusion with the highest quality IFU data now available with KMOS^{3D} on subgalactic scales, over a wider redshift and mass range than previously, and using a sample purely selected on the basis of disk galaxies near the main sequence at each redshift. We further put our results into the broader literature context, including multiphase gas velocity dispersion and expanding the redshift range to $0 < z < 4$.

4.1. The KMOS^{3D} Velocity Dispersions from $z = 2.6$ to $z = 0.6$

In Figure 4, we show the intrinsic velocity dispersion of our KMOS^{3D} galaxies in the kinematic sample as a function of redshift, where upper limits are indicated by arrows (Section 3.4). Our data reflect the known trend of increasing average velocity dispersions with increasing redshift.

To quantify the evolution, we fit a linear relation in σ_0 - z space to our best-fit data.¹⁸ We use the Bayesian approach to linear regression by Kelly (2007), which allows for the inclusion of censored data (i.e., upper limits). The routine requires symmetric uncertainties, which we calculate as the mean of the asymmetric uncertainties on σ_0 from our MCMC modeling.¹⁹ Figure 4 shows the derived fit as a solid line, with average values of $\sigma_0 \sim 31.1, 38.3,$ and 46.7 km s^{-1} at $z \sim 0.9, 1.5,$ and 2.3 . The corresponding fit is described by the equation

$$\sigma_0 [\text{km s}^{-1}] = (21.1 \pm 3.0) + (11.3 \pm 2.0) \cdot z. \quad (1)$$

¹⁸ Our results do not depend on this particular functional form, and we list fits in $\sigma_0 - \log(1+z)$ and $\log(\sigma_0) - \log(1+z)$ space in Appendix B.

¹⁹ We assume an uncertainty on z of five times the spectral resolution in each redshift bin, translating into (negligible) uncertainties of $\delta z \sim 0.001$ – 0.002 .

We also perform a “robust” fit where the upper limit cases are not included, but entirely left out. We find a slightly shallower evolution indicated by the dashed line. If, instead, for these galaxies we do not assign upper limits but take the formal median of the posterior distribution at face value, we find a slightly steeper evolution indicated by the dashed-dotted line. In Table 3, we list our fit parameters and uncertainties.

The σ_0 evolution we derive between $z \sim 0.9$ and $z \sim 2.3$ is slightly shallower than what has been reported for the first year of data from the KMOS^{3D} survey by Wisnioski et al. (2015). In particular, the authors cite $\sigma_0 \sim 24.9 \text{ km s}^{-1}$ at $z \sim 0.9$ and $\sigma_0 \sim 47.5 \text{ km s}^{-1}$ at $z \sim 2.3$, i.e., a difference of 6 – 7 km s^{-1} for the lowest redshift bin. We partly attribute this difference to our treatment of upper limits. Indeed, if we take the formal best-fit values of the upper limit cases at face value, we find through linear regression a value of $\sigma_0 \sim 28.4 \text{ km s}^{-1}$ at $z \sim 0.9$ (see Table 3), reducing the difference to $\sim 4 \text{ km s}^{-1}$. This difference is smaller than the uncertainty on the average σ_0 value we derive through our fitting based on the standard deviation of the posterior distribution of the zero point and slope, which is $\delta\sigma_0 = 4.8 \text{ km s}^{-1}$ for the $z \sim 0.9$ bin.

4.2. Quantification of Observational Uncertainties and the Scatter in σ_0

Figure 4 shows substantial scatter in σ_0 at fixed redshift with values from $\sigma_0 \approx 20 \text{ km s}^{-1}$ to $\sigma_0 \approx 100 \text{ km s}^{-1}$. The question is whether this scatter is physical or purely driven by observational uncertainties.

As listed in Table 3, our robust best-fit relation has an intrinsic scatter around the regression with a standard deviation of 10.4 km s^{-1} , suggesting that part of the scatter is indeed due to real variations of the intrinsic dispersion values and not just due to measurement uncertainties. To quantify the intrinsic variance in each redshift slice, we first calculate the observed variance around the robust best-fit relation, i.e., the variance of the redshift-normalized dispersion values excluding upper limits. The redshift-normalized values are defined as

$$\sigma_{0,\text{norm}} = \sigma_0 - (a + b \cdot z), \quad (2)$$

with coefficients a and b as listed in Table 3. Then, we perform a Monte Carlo analysis of the scatter due to uncertainties: for each measurement i , we draw 1000 times from a normal distribution $\mathcal{N}(0, \delta\sigma_{0,i})$, where $\delta\sigma_{0,i}$ is the symmetric uncertainty of $\sigma_{0,i}$ derived from our DYSMAL MCMC modeling and calculate the corresponding sample variance per redshift slice.

We calculate this intrinsic variance as

$$\text{VAR}_{\text{int}}(z) = \text{VAR}_{\text{obs}}(z) - \text{VAR}_{\delta\sigma_0}(z) \quad (3)$$

and list the corresponding values in Table 4. From this analysis, we conclude that at least $\sim 40\%$ – 50% of the observed variance, i.e., $\sim 60\%$ – 70% of the observed scatter, is due to real variations of the intrinsic dispersion values, mostly independent of redshift. We also show a histogram of the redshift-normalized dispersion values in Figure 5, $\sigma_{0,\text{norm}}$, in black, together with a histogram of the Monte Carlo draws from the uncertainty distribution in red. Again, this clearly shows that, even though the uncertainties are substantial, there is residual scatter in our σ_0 distribution beyond what can be accounted for by uncertainties. Further, if we focus on the absolute values listed in Table 4, the intrinsic variance increases above $z \sim 1.5$,

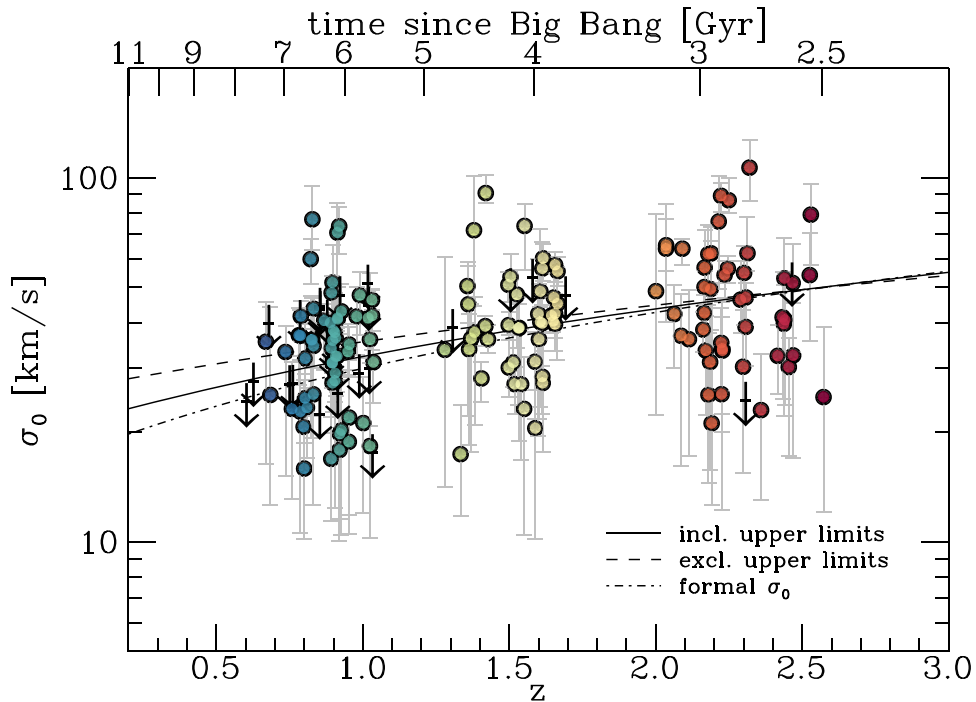


Figure 4. Intrinsic velocity dispersion σ_0 as a function of redshift and cosmic time for our kinematic sample, color-coded by redshift. Upper limits are shown by black arrows. On average, σ_0 increases with redshift, but the scatter at fixed redshift is large. The solid line shows the linear regression including the upper limits. The dashed line shows a corresponding fit for which the upper limit cases have been entirely excluded, resulting in a slightly shallower evolution. Taking the formal fit results for all galaxies at face value, we find a slightly steeper evolution (dashed-dotted line).

Table 3

Results from the Linear Regression Fits of the Form $\sigma_0/\text{km s}^{-1} = a + b \cdot z + c$ for Our Kinematic Sample, where a and b are the Regression Coefficients, and c is the Intrinsic Random Scatter about the Regression (See Kelly 2007)

Sample	N	a	b	σ_c	l_{corr}	σ_0 at $z \sim 0.9$ (km s^{-1})	σ_0 at $z \sim 1.5$ (km s^{-1})	σ_0 at $z \sim 2.3$ (km s^{-1})
Including Upper Limits	175	21.1 ± 3.0	11.3 ± 2.0	11.3 ± 1.1	0.51 ± 0.08	31.1	38.3	46.7
Excluding Upper Limits (Robust)	147	26.2 ± 3.1	9.2 ± 2.1	10.4 ± 1.1	0.46 ± 0.09	34.3	40.3	47.1
Using Formal Best-fit σ_0	175	17.2 ± 3.2	12.7 ± 2.2	13.2 ± 1.1	0.49 ± 0.07	28.4	36.7	46.1

Note. For each parameter a and b , the standard deviation of c , and the derived linear correlation coefficient l_{corr} between σ_0 and z , we list the median together with the standard deviation of the posterior distribution. For each redshift slice, we list the best-fit σ_0 value corresponding to these medians.

such that at $z \sim 2.3$, it has doubled compared to $z \sim 0.9$ and $z \sim 1.5$. This suggests that the population of galaxies in our highest redshift bin is more diverse in ISM conditions compared to the lower redshift samples.

However, no significant residual trend with $\sigma_{0,\text{norm}}$ and the physical properties related to SFR, mass, size, or rotation velocity remains, as we show in detail in Figure 15 in Appendix C. That means that we cannot identify a physical source for the scatter in σ_0 at fixed redshift. This might be due to the limited dynamical range of our data, or it could imply that the intrinsic scatter is driven through the interplay of more than one parameter. Alternatively, the scatter could be due to real variations of the velocity dispersion on short timescales, for instance caused by a dynamic driver such as minor mergers or variations in gas accretion from the cosmic web. This has recently been proposed by Hung et al. (2019) based on results from the FIRE simulations, where variations of the intrinsic

dispersion are connected to variations of the gas inflow rate on timescales $\lesssim 100$ Myr.

4.3. Comment on the Effect of Sample Selection

The results presented above and in the remainder of the paper are based on our kinematic sample as defined in Section 3.3, i.e., 175 resolved and rotation-dominated disk galaxies that are well fit by our dynamical model, without strong contamination from OH lines or outflows, and without close neighbors. If we instead consider all modeled galaxies from setup 1, which is about twice as many compared to the kinematic sample (see Section 3.2), we find a similar median evolution of $\sigma_0 \approx 31, 40$, and 49 km s^{-1} at $z \sim 0.9, 1.5$, and 2.3 ; however, the mean values in the three redshift slices are systematically higher with $\sigma_0 \approx 34, 45$, and 58 km s^{-1} . While at all redshifts the scatter is substantially increased due to galaxies with higher observational uncertainties or poor fits

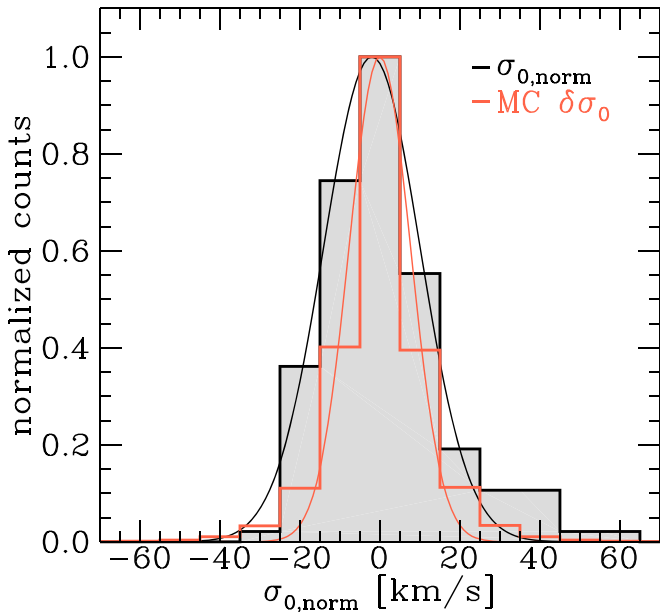


Figure 5. Histogram of redshift-normalized intrinsic dispersion values, $\sigma_{0,\text{norm}}$, in black, and histogram of the contribution to the scatter from uncertainties based on a Monte Carlo analysis in red (see Section 4.2 for details). To guide the eye, we show the simple Gaussian fits to the two distributions by the thin curves. There is excess scatter beyond what can be accounted for by uncertainties in the distribution of $\sigma_{0,\text{norm}}$, indicating that we observe real physical variations of σ_0 at fixed redshift (see also Table 4).

Table 4

Variances of σ_0 around the Robust Best-fit Relation: Observed Variance VAR_{obs} , Variance Due to Measurement Uncertainties, $\text{VAR}_{\delta\sigma_0}$, and Intrinsic Variance, VAR_{int}

Measure	$z \sim 0.9$	$z \sim 1.5$	$z \sim 2.3$	$0.6 < z < 2.6$
$\text{VAR}_{\text{obs}} (\text{km}^2 \text{s}^{-2})$	171	208	357	237
$\text{VAR}_{\delta\sigma_0} (\text{km}^2 \text{s}^{-2})$	87	130	194	133
$\text{VAR}_{\text{int}} (\text{km}^2 \text{s}^{-2})$	85	78	163	104
$\text{VAR}_{\text{int}}/\text{VAR}_{\text{obs}}$	0.50	0.38	0.46	0.44

($\text{VAR}_{\text{obs}} \approx 730, 850, \text{ and } 1560 \text{ km}^2 \text{ s}^{-2}$), the systematic increase of the mean values is mostly due to the inclusion of dispersion-dominated systems (see, e.g., Newman et al. 2013 for a discussion of such galaxies).

4.4. Multiphase Velocity Dispersions from $z = 4$ to $z = 0$

To put the evolution of velocity dispersion from $z = 2.6$ to $z = 0.6$ based on our KMOS^{3D} sample into a broader context, we collect measurements reported in the literature from $z \sim 4$ to $z = 0$, covering 12 Gyr of cosmic history (Table 5).

In the top panel of Figure 6, we show again our KMOS^{3D} kinematic sample as clouds of gray circles, including upper limits as arrows, in the σ_0 - z space. The median values at $z \sim 0.9, 1.5, \text{ and } 2.3$, shown as large circles in blue, green, and red, are based on the best fit plotted in Figure 4 and its uncertainties (see Table 3). We include other individual intrinsic dispersion measurements or averages from ionized gas as colored symbols, and atomic and molecular data as black symbols, which are listed in Table 5. Error bars show the mean uncertainty of the individual systems in those samples. In our comparison, we do not apply any corrections or normalizations

in mass (see Wisnioski et al. 2015), which are expected to be small for main-sequence galaxies (Simons et al. 2017).

In Table 5, we also list the different techniques used to correct for beam-smearing effects. As explained in Section 3.2 and in the references listed there, we account for beam-smearing effects through a full forward-modeling of both the velocity and velocity dispersion fields with a unique PSF model for each galaxy. Techniques based on only the velocity information, or on grid-based models or look-up tables, might perform less well in their beam-smearing corrections generally resulting in overestimated intrinsic velocity dispersions. For slit surveys, systematic offsets toward higher values might be expected, due to the sometimes uncertain galaxy position angle and the resulting difficulties in disentangling rotational and turbulent motions (see Price et al. 2016, 2019 for a discussion and solution approach). Similarly, the methods chosen to calculate or model the intrinsic velocity dispersion might further introduce systematic differences. We note that recent work by Varidel et al. (2019) on a sample of 20 local SFGs suggests that complex structure in the gas distribution may further impact the derived dispersion values.

Figure 6 shows generally good agreement of the various σ_0 measurements reported in the literature. Comparing slit versus IFU techniques, the slit measurements shown here, i.e., data from DEEP2, SIGMA, and MOSDEF, tend toward higher values compared to the averages derived from our KMOS^{3D} and SINS/zC-SINF surveys, likely for the reasons discussed above, but agree within their uncertainty with the IFU data where available. Interestingly, the deep measurements obtained for individual targets by Genzel et al. (2017), and particularly for the lensed systems by Livermore et al. (2015) and Jones et al. (2010) at $1.5 < z < 3$ also tend toward higher σ_0 values, but have moderate values at $z > 3$, in agreement with the averages obtained from seeing-limited IFU and slit spectroscopy by Gnerucci et al. (2011), Turner et al. (2017), and Price et al. (2019). Generally, the statistical power of these time-intensive and challenging individual measurements is still very limited. Systematic differences in σ_0 may arise through selection effects: for instance, the nearby galaxies from the DYNAMO sample are selected to be $z \sim 2$ analogs and have many physical properties, including dispersions, similar to high- z SFGs (see Green et al. 2014; White et al. 2017; Fisher et al. 2019).

In contrast, the molecular and atomic data indicated by black points suggest somewhat lower values on average, particularly at $z \approx 0$. Levy et al. (2018) study 17 nearby, rotation-dominated SFGs in CO and ionized gas. They found consistently higher rotation velocities ($\langle v_{\text{CO}} - v_{\text{H}\alpha} \rangle \approx 14 \text{ km s}^{-1}$) and lower velocity dispersions ($\langle \sigma_{\text{CO}} - \sigma_{\text{H}\gamma} \rangle \approx -17 \text{ km s}^{-1}$) for the molecular gas compared to the ionized gas (see also Cortese et al. 2017 for a comparison at $z \sim 0.2$). At high redshift, there exist only few multiphase measurements of the intrinsic gas velocity dispersion. Detailed observations reveal comparable values for ionized and molecular gas (Genzel et al. 2013; Übler et al. 2018); however, the uncertainties are larger such that differences like those found locally could be washed out.

4.5. Multiphase Gas Velocity Dispersions Evolve Similarly with Redshift

We quantify the difference between the atomic+molecular and the ionized gas velocity dispersions over cosmic time in the bottom panel of Figure 6. Fitting a robust linear relation²⁰ to the average

²⁰ We use the least trimmed squares method by Cappellari et al. (2013).

Table 5
Literature Data of the $0 < z < 4$ Velocity Dispersion Measurements Shown in Figure 6

Sample/ References	z	Primary Tar- get Line	N Included	Instrument/Method	BS Correction	Comment on Selection
KDS	3.8–3.1	[O III]	14	KMOS/IFU	(1)	their “RD”
MOSDEF	3.8–1.4	H α , H β , [O III]	108	MOSFIRE/slit	(2)	their “resolved/aligned”
AMAZE-LSD	3.7–3.1	[O III]	11	SINFONI/IFU	(1)	their “rotating”
Livermore et al. (2015)	3.7–1.3	H α , H β	8	SINFONI+NIFS+OSIRIS/ IFU+lensing	(3)	their “Disk” with $v_{\text{rot}}/\sigma_0 > 1$
KMOS ^{3D}	2.6–0.6	H α	175	KMOS/IFU	(2)	see Section 3.3
SINS/zC-SINF	2.5–1.4	H α	25	SINFONI/IFU+AO	(2)	see Section 3.3
SIGMA	2.5–1.3	H α , [O III]	49	MOSFIRE/slit	(4)	
Genzel et al. (2017)	2.4–0.9	H α	6	KMOS+SINFONI/IFU+AO	(2)	see Section 3.3
MASSIV	1.6–0.9	H α , [O III]	53	SINFONI/IFU	(1)	
DEEP2	1.2–0.1	H α , H β , [O II], [O III]	544	DEIMOS/slit	(4)	
KROSS	1.0–0.8	H α	171	KMOS/IFU	(4)	their “sigma0_flag = O” with $v_{2.2}/\sigma_0 > 1$
DYNAMO	~ 0.1	H α	25	SPIRAL+WiFeS/IFU	(1)	their “RD”
GHASP	local	H α	153	scanning Fabry–Perot	(1)	
Übler et al. (2018)	1.4	H α , CO(3–2)	1	LUCI/slit+NOEMA/ interferometry	(2)	see Section 3.3
Swinbank et al. (2011)	2.4	CO (6–5), CO(1–0)	1	IRAM+EVLA/ interferometry	(3)	
PHIBSS	1.5–0.7	CO(3–2)	7	IRAM+NOEMA/ interferometry	(4)	see Section 3.3
HERACLES	local	CO(2–1)	13	IRAM/single dish	(5)	
EDGE-CALIFA	local	CO(1–0)	17	CARMA/interferometry	(1)	
THINGS	local	H I	35	VLA/interferometry	(5)	
Dib et al. (2006)	local	H I	13	literature compilation		

Note. Beam-smearing (BS) correction methods: (1) correction map derived from the model velocity field including two-dimensional PSF, (2) simultaneous forward-modeling of both the velocity and dispersion including two-dimensional PSF; see Section 3.2, (3) subtraction in quadrature of the velocity gradient across each spaxel, (4) model-based look-up grid, and (5) exclusion of regions most strongly affected based on a model grid.

References. KDS, Turner et al. (2017); MOSDEF, Kriek et al. (2015); Price et al. (2019); AMAZE-LSD, Gnerucci et al. (2011); KMOS^{3D}, Wisnioski et al. (2015; E. Wisnioski et al. 2019, in preparation); SINS/zC-SINF, Förster Schreiber et al. (2006, 2009, 2018); SIGMA, Simons et al. (2016, 2017); MASSIV, Contini et al. (2012), Epinat et al. (2012); DEEP2, Davis et al. (2003), Kassin et al. (2007, 2012); KROSS, Stott et al. (2016), Johnson et al. (2018); DYNAMO, Green et al. (2014); GHASP, Epinat et al. (2008, 2010); PHIBSS, Tacconi et al. (2013), Freundlich et al. (2019); HERACLES, Leroy et al. (2009), Tamburro et al. (2009), Caldú-Primo et al. (2013), Mogotsi et al. (2016); EDGE-CALIFA, Bolatto et al. (2017), Levy et al. (2018); THINGS, Walter et al. (2008), Tamburro et al. (2009), Ianjamasimanana et al. (2012), Caldú-Primo et al. (2013), Mogotsi et al. (2016).

local and individual high- z measurements of atomic+molecular gas, we find a zero point of $a = 10.9 \pm 0.6 \text{ km s}^{-1}$ and a slope of $b = 11.0 \pm 2.0 \text{ km s}^{-1}$ (gray dashed line). For the ionized velocity dispersion, we choose in addition to our own averages from the KMOS^{3D} and SINS/zC-SINF surveys the other large KMOS surveys, KROSS and KDS, and the local average from the GHASP survey. This choice maximizes the redshift range and avoids systematic effects at $z > 0$ through different instrumentation. We find a higher zero-point offset of $a = 23.3 \pm 4.9$ and a somewhat shallower slope of $b = 9.8 \pm 3.5$, while the extrapolation of our best fit to the KMOS^{3D} data only gives $a = 21.1 \pm 3.0$ and $b = 11.3 \pm 2.0$ (Table 3). Fixing the slope to that of the atomic+molecular fit, the zero point shifts in between these measurements, with $a = 22.8$. In Table 6, we list our fit parameters and uncertainties.

This suggests that the redshift evolution of the intrinsic velocity dispersion in all gas phases is quite comparable, but their normalization differs. The typical thermal broadening of the atomic/molecular and the ionized gas due to their characteristic temperatures is $\sim 5 \text{ km s}^{-1}$ and $\sim 10 \text{ km s}^{-1}$, respectively, meaning the measured velocity dispersions are superthermal even in the local universe. Part of the difference between atomic+molecular and ionized gas velocity

dispersions can be explained through the expansion of H II regions from which the ionized emission originates, with typical values of $10\text{--}25 \text{ km s}^{-1}$ (Shields 1990), accounting for another $\sim 5\text{--}15 \text{ km s}^{-1}$ when added in quadrature. In combination, these effects can explain the difference in the local normalizations of the gas-phase velocity dispersions, as well as their average offset of $\sim 10\text{--}15 \text{ km s}^{-1}$ at fixed redshift.

Clearly, more studies of high- z molecular kinematics are warranted to corroborate our result, which potentially has important implications for work on ionized gas kinematics.

4.6. Comments on Thin versus Thick Disk Evolution

Figure 6 shows a smooth evolution of velocity dispersion with redshift over the past ~ 12 Gyr, likely connected to decreasing accretion rates and gas fractions with cosmic time (see Sections 5.3 and 5.4). This evolution also suggests that the typical thickness of the young, star-forming gas disk is lower for lower redshift SFGs, as has also been found in state-of-the-art cosmological simulations (Pillepich et al. 2019).

This is potentially interesting in the context of Galactic archeology: early research of the vertical structure of our Milky Way found evidence for two main, distinct exponential disks with

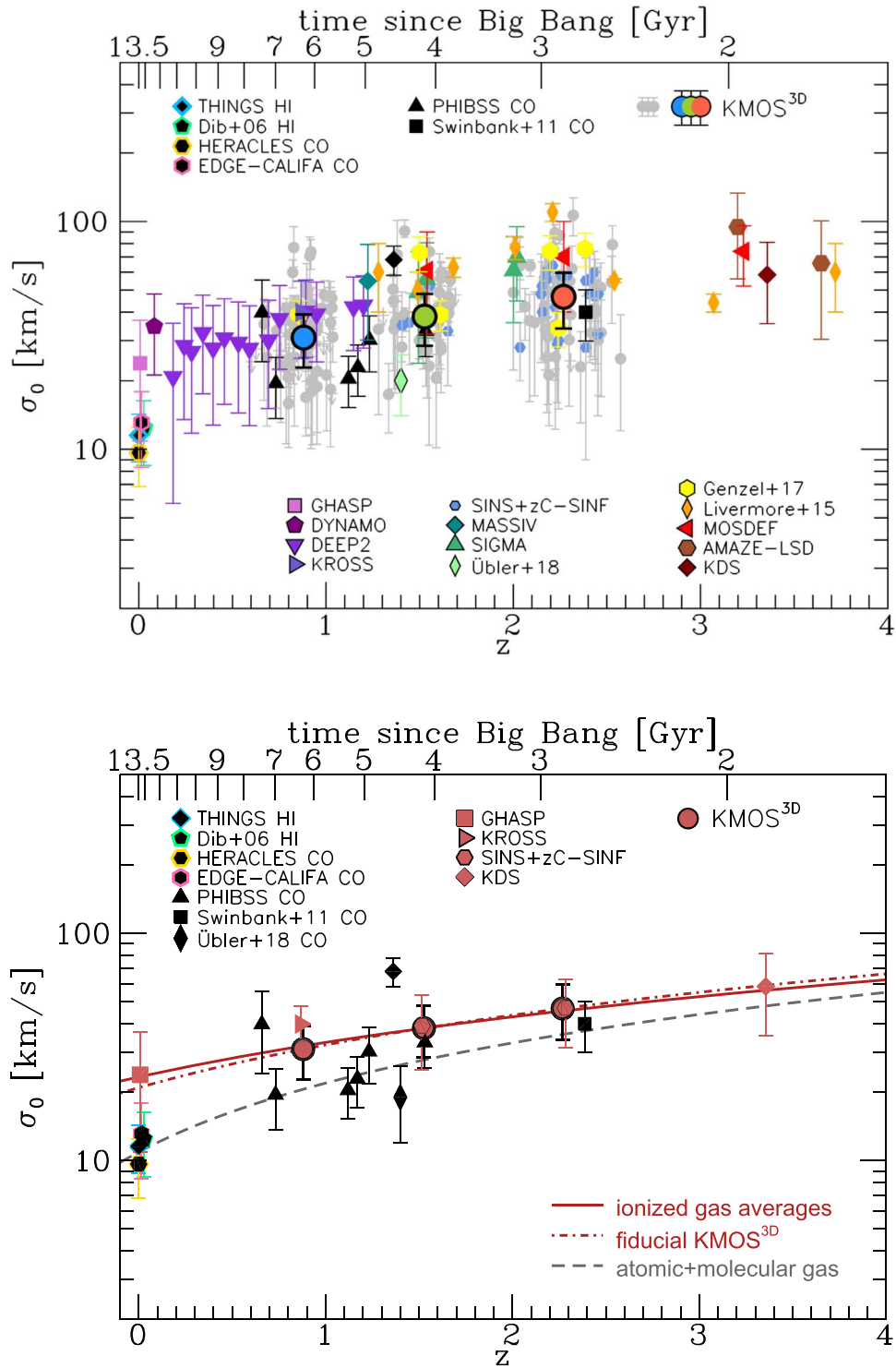


Figure 6. Intrinsic velocity dispersion σ_0 as a function of redshift and cosmic time for measurements from the literature at $0 < z < 4$ (see Table 5). Top: our kinematic sample is shown in gray, with colored averages. Other individual and average ionized gas measurements are shown in color, as indicated in the legend. Molecular and atomic gas measurements are shown in black. For averages, the error bar shows the typical uncertainty of individual measurements in the sample. Bottom: averages from selected ionized gas measurements are shown in red. Local atomic and molecular averages and individual high- z molecular gas measurements are shown in black. Based on these data, we show best-fit relations (see Table 6) for molecular gas (gray dashed) and ionized gas (red solid), as well as the best fit derived solely based on our KMOS^{3D} data (red dashed-dotted line; see Section 4.1 and Table 3). Confirming the trend seen in our kinematic sample for the redshift range $0.6 < z < 2.6$, σ_0 increases with redshift over a time span of almost 12 Gyr. In the local universe, velocity dispersions measured from molecular or atomic gas are lower than corresponding measurements from ionized gas, by about 10–15 km s⁻¹. The slopes derived from the molecular data and from our KMOS^{3D} sample are almost identical, suggesting an analogous redshift evolution of the different gas-phase velocity dispersions.

scale heights of ~ 300 and ~ 1450 pc (Gilmore & Reid 1983). This was confirmed through later work on the Milky Way as well as nearby edge-on galaxies (e.g., Dalcanton & Bernstein 2002;

Yoachim & Dalcanton 2006; Jurić et al. 2008). The thick disk components have been found to be generally older (>6 Gyr) than those of the thin disks, raising the question of distinct formation

Table 6

Results and Standard Deviations from the Robust Least-squares Linear Regression Fits of the Form $\sigma_0/\text{km s}^{-1} = a + b \cdot z$ to the Data Sets Shown in the Bottom Panel of Figure 6

Sample	a (km s ⁻¹)	b (km s ⁻¹)
Ionized Gas (Best Averages)	23.3 ± 4.9	9.8 ± 3.5
... Fixing Slope to Atomic+Molecular	22.8	11.0 (fixed)
KMOS ^{3D} Incl. Upper Limits (Table 3)	21.1 ± 3.0	11.3 ± 2.0
Atomic+Molecular Gas	10.9 ± 0.6	11.0 ± 2.0

periods. Naturally, observations of the typically thick high- z disks also prompted the question of the connection between these early thick disks and modern disk structure (e.g., Elmegreen & Elmegreen 2006).

To explicitly address the question of distinct formation periods of thin versus thick disks, we make the simple assumption of a step function describing the σ_0 of the ionized gas below and above $z = 1$. Unsurprisingly, the resulting fit with $\sigma_0 = 28 \text{ km s}^{-1}$ at $z < 1$ and $\sigma_0 = 42 \text{ km s}^{-1}$ at $z > 1$ is not a good description of the compiled data, with a goodness of fit that is a factor of ~ 20 worse compared to the linear fit shown in the bottom panel of Figure 6.

Our results suggest that in the absence of recent major mergers, it should depend primarily on the star formation history (connected to gas accretion) if present-day galaxies have distinct disks of different age and scale height, or if there is instead one component with a vertical age gradient (see also Leaman et al. 2017). This interpretation is in agreement with the recent work by Bovy et al. (2012, 2016) and Rix & Bovy (2013), who argue based on elemental abundances that the Milky Way has a continuous range of different scale heights, with no sign of a thin–thick disk bimodality. Simulations by, e.g., Burkert et al. (1992), Aumer et al. (2016), Aumer & Binney (2017), and Grand et al. (2016) support this picture.

However, in this context, it is important to remember that based on the stellar and gas masses of our galaxies and results from comoving number density studies (e.g., Brammer et al. 2011), only the lower mass, lower redshift systems in our sample may evolve into present-day disk galaxies, while the galaxies that already have high baryonic masses at high redshift will most likely evolve into present-day’s early-type galaxies. With our data, we, therefore, do not necessarily track the change in star-forming scale height over time for progenitor–descendant populations, but rather the change in average star-forming scale height of main-sequence galaxies at different epochs.

5. What Drives the Gas Velocity Dispersion?

5.1. Galaxy-scale Velocity Dispersion Correlates with Gas Mass and SFR Properties

The redshift dependence of σ_0 suggests that one or more physical galaxy properties that are themselves redshift-dependent drive velocity dispersion. Consistent with previous findings in the literature (e.g., Johnson et al. 2018), we find several properties positively correlating with σ_0 , particularly the SFR, SFR surface density Σ_{SFR} , gas and stellar mass, and their surface densities. We list direct and residual (after correcting for redshift dependence) Spearman rank correlations in Table 7 and show plots for several quantities in Figure 16 in Appendix C. In Table 7, we also list the $\text{SFR}_{\text{H}\alpha}$ and $\Sigma_{\text{SFR},\text{H}\alpha}$ derived from the H α fluxes (see E. Wisnioski et al. 2019, in

Table 7

Spearman Rank Correlation Coefficients, ρ_S , and Their Significance, σ_ρ , between σ_0 and Different Galaxy Properties for Our Robust Sample before and after Accounting for the Redshift Dependence of σ_0

Quantity	$\sigma_0(z)$		$\sigma_{0,\text{norm}}$	
	ρ_S	σ_ρ	ρ_S	σ_ρ
z	0.33	4.0
SFR	0.38	4.6	0.18	2.1
$\text{SFR}_{\text{H}\alpha}$	0.36	4.4	0.14	1.7
Σ_{SFR}	0.32	3.9	0.06	1.0
$\Sigma_{\text{SFR},\text{H}\alpha}$	0.30	3.7	0.08	0.9
M_{gas}	0.38	4.6	0.19	2.3
Σ_{gas}	0.31	3.8	0.07	0.9
M_*	0.26	3.1	0.20	2.4
Σ_*	0.26	3.1	0.14	1.6
M_{bar}	0.32	3.9	0.20	2.4
Σ_{bar}	0.30	3.6	0.12	1.5
ΔMS	0.15	1.8
ΔMR	-0.05	0.6

preparation), tracing the more recent star formation history, but find no appreciable difference in correlations compared to our fiducial SFR properties (see Section 2).

We emphasize that due to the limited dynamical range covered by the individual redshift slices, we do not find significant correlations of σ_0 within one redshift slice with any of the above properties, such that we cannot readily connect the scatter in σ_0 at fixed redshift to a physical driving source. Similarly, if we remove the redshift dependence of σ_0 by normalizing with our best-fit relation, we do not find any significant correlations of the normalized σ_0 with physical properties (see Section 4.2 and Figure 15).

Over the full redshift range covered by our KMOS^{3D} survey, the SFR and gas mass correlate most strongly and significantly with intrinsic velocity dispersion. In order to identify which of these two physical quantities is most directly tied to the elevated velocity dispersions at high redshift, we discuss in the following sections the physical mechanisms through which quantities such as SFR and gas mass may affect velocity dispersion, namely stellar feedback and gravitational instabilities, and we comment on the tentative connection to active galactic nucleus (AGN) feedback for individual galaxies.

5.2. Stellar Feedback

Turbulence driving can be provided through thermal and momentum feedback from massive stars. Correlations between intrinsic velocity dispersion and SFR properties have previously been reported in the literature (e.g., Dib et al. 2006; Lehnert et al. 2009, 2013; Green et al. 2010, 2014; Moiseev et al. 2015; Johnson et al. 2018), and often invoked the argument for stellar feedback-driven turbulence.

From a theoretical point of view, feedback-driven turbulence is mainly generated through momentum injection from supernovae into the ISM (contributions to the momentum injection from, e.g., expanding H II regions or stellar winds are minor; see Mac Low & Klessen 2004; Ostriker & Shetty 2011). Feedback-driven turbulence should therefore primarily depend on the decay rate of turbulence, the momentum injected per supernova, and the supernova rate, where the latter is the quantity connecting turbulence to the SFR and Σ_{SFR} . Ostriker & Shetty (2011) and Shetty & Ostriker (2012) derived a weak

dependence of σ_0 on star formation rate surface density. Even considering the case where feedback-driven turbulence vertically stabilizes the disk, the resulting velocity dispersions are low (Equation (22) by Ostriker & Shetty 2011):

$$\sigma_z = 5.5 \text{ km s}^{-1} \cdot \frac{f_p}{(1 + \chi)^{1/2}} \left(\frac{\epsilon_{\text{ff}}(\rho_0)}{0.005} \right) \left(\frac{p_*/m_*}{3000 \text{ km s}^{-1}} \right). \quad (4)$$

Here, f_p is a factor characterizing the evolution of turbulence, with $f_p = 1$ for strong dissipation and $f_p = 2$ for weak dissipation. χ is a measure of the importance of the gas disk's self-gravitational weight and is below 0.5 for marginally stable disks, such that the first factor is in the range ~ 0.8 –2. The mean star formation efficiency $\epsilon_{\text{ff}}(\rho_0)$ is assumed to be approximately constant with a fiducial value of $\epsilon_{\text{ff}}(\rho_0) = 0.005$. $p_*/m_* = 3000 \text{ km s}^{-1}$ is the fiducial value of momentum injection per supernova (but see, e.g., Fisher et al. 2019 for arguments for a z -dependent p_*/m_*). As a result, the gas velocity dispersion is expected to vary only mildly due to supernova explosions.

Similar results are obtained by other theoretical models investigating stellar feedback as the sole driver of the turbulence in the ISM, for instance the models discussed by Dib et al. (2006), Joung et al. (2009), and Kim et al. (2013). In fact, the resulting velocity dispersions in the ISM do not even seem to depend much on the supernova rate. Rather, very high supernova rates might create superbubble structures that, instead of stirring the ambient medium, will eventually blow out of the galactic disk, thus transferring energy and metals into the circumgalactic medium (Mac Low et al. 1989; Joung et al. 2009; Baumgartner & Breitschwerdt 2013; Kim & Ostriker 2018). This is an important result because at higher redshift, the supernova rate is also higher. However, other work indicates that it is not only the rate but also the location of supernovae that is crucial for the efficiency of stellar feedback turbulence driving: considering peak driving, where supernovae go off in the densest ISM regions (e.g., their birth clouds), Gatto et al. (2015) found local H α velocity dispersions of up to 60 km s^{-1} for gas mass surface densities of $\Sigma_{\text{gas}} \sim 100 M_\odot \text{ pc}^{-2}$. This is similar to high- z conditions and therefore suggests that stellar feedback can more easily maintain elevated velocity dispersions at higher redshift. Also, some idealized simulations of isolated galaxies are able to produce a velocity dispersion of $\sim 50 \text{ km s}^{-1}$ from strong stellar feedback (Hopkins et al. 2011).

If stellar feedback is an important factor in powering turbulence, then it would not only be the (observed) global scaling of velocity dispersion with SFR or Σ_{SFR} that will be expected, but in particular locally elevated velocity dispersion in regions of high star formation rate density (see Gatto et al. 2015). We exploit the high-resolution data from the SINS-zC/SINF AO survey (Förster Schreiber et al. 2018) to study local correlations between Σ_{SFR} and σ_0 . In Figure 7 we show the local intrinsic velocity dispersion per spaxel of galaxy Q2346-BX482 as a function of radius, color-coded by Σ_{SFR} (adopted from Figure A1 by Genzel et al. 2011). The local intrinsic velocity dispersion is derived from the observed dispersion map, after correcting all instrumental and beam-smearing effects through modeling. In the vicinity of the giant star-forming clump $\sim 6.5 \text{ kpc}$ southeast from the center (inset), no elevated velocity dispersion can be registered.

In Figure 8, we show the local intrinsic velocity dispersion per spaxel as a function of local Σ_{SFR} for 10 SINS/zC-SINF galaxies. The velocity dispersions of these galaxies with a

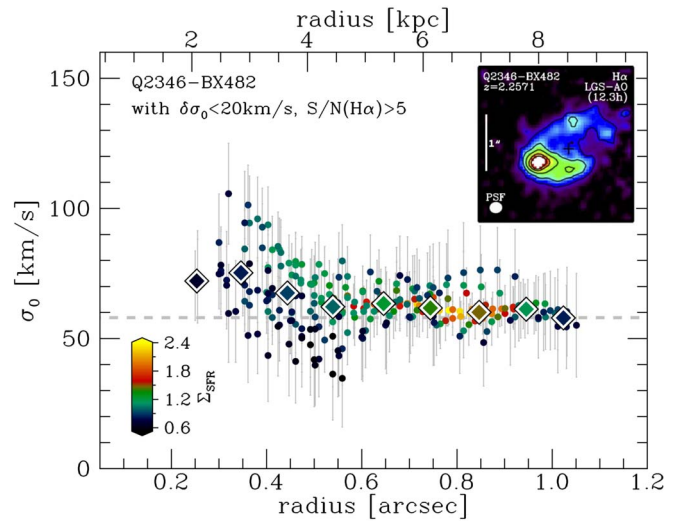


Figure 7. Intrinsic local velocity dispersion σ_0 as a function of radius for galaxy Q2346-BX482, measured from individual spaxels (circles) and color-coded by local Σ_{SFR} (adopted from Figure A1 by Genzel et al. 2011). Larger diamonds show the running median. The gray dashed line shows the best-fit intrinsic velocity dispersion from kinematic modeling where σ_0 is assumed to be constant. The inset in the top-right corner shows the projected map of H α flux, featuring the bright star-forming clump to the southeast, adopted from Figure 16 by Förster Schreiber et al. (2018). There is no correlation between local Σ_{SFR} and local velocity dispersion.

mean redshift of $z \sim 2.2$ have somewhat higher values compared to our KMOS^{3D} sample, consistent with their higher average SFR and Σ_{SFR} . Only two of these galaxies show an intrinsic scaling of σ_0 with Σ_{SFR} . The best-fit power-law relation derived from this subgalactic, high-quality data shows a very weak dependence of local σ_0 on Σ_{SFR} ,²¹ confirming the earlier findings by Genzel et al. (2011); see also Patrício et al. 2018; Tadaki et al. 2018; but see Swinbank et al. 2012a). Similar results are found for both ionized gas (Varidel et al. 2016; Zhou et al. 2017) and molecular gas (Caldú-Primo & Schrubba 2016) in local galaxies. For atomic gas, several studies of local galaxies find correlations with SFR or Σ_{SFR} that are too weak to explain the turbulent velocities in the galaxy outskirts (e.g., Tamburro et al. 2009; Ianjamasimanana et al. 2015; Utomo et al. 2019).

In summary, while global σ_0 correlates with SFR properties, we do not find a direct connection between high, local star formation activity and elevated σ_0 , as suggested by some simulations. Generally, however, simulations and models agree that stellar feedback is able to maintain galaxy-wide turbulence on scales of 10 – 20 km s^{-1} .

5.3. Marginally Toomre-stable Disks

Turning to gravity-driven turbulence, an empirical model to describe the redshift evolution of velocity dispersion is that of marginally stable disks, where (non-interacting) galaxies are subject to gas replenishment from the halo or the cosmic web, and to gas loss through either outflows or star formation (Noguchi 1999; Silk 2001; Immeli et al. 2004a, 2004b; Förster

²¹ This finding does not extend to nuclear regions, because more complex circumnuclear kinematic structure caused by a combination of nuclear outflows, radial inflow, and bulge-induced rotation in a number of cases generates unresolved velocity fields that appear as an increased velocity dispersion. To explore its true nature will require <0.1 IFU spectroscopy on 30 m class telescopes.

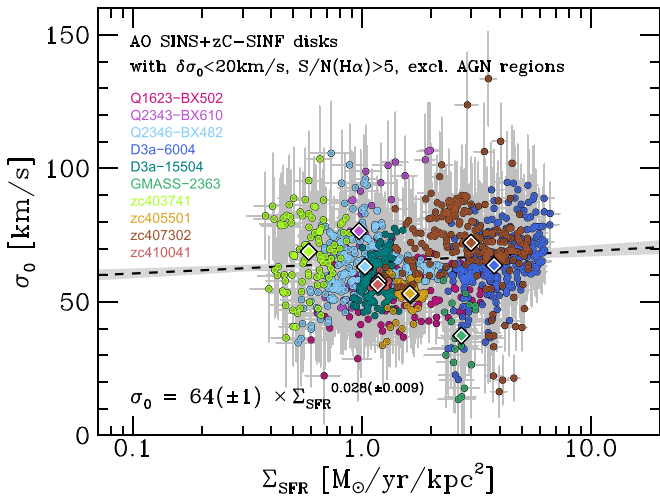


Figure 8. Intrinsic local velocity dispersion σ_0 as a function of star formation rate surface density Σ_{SFR} , measured from individual spaxels in 10 galaxies from the SINS/zC-SINF survey adaptive optics follow-up. We select spaxels with $\delta\sigma_0 < 20 \text{ km s}^{-1}$, $S/N(\text{H}\alpha) > 5$, and exclude the regions of three galaxies that are affected by AGN feedback. Colored circles correspond to data from the different galaxies as listed in the legend, and larger diamonds show the median values. The black dashed line shows the linear regression to the individual spaxel data, with fit uncertainties shown as gray shading, as given in the bottom of the figure.

Schreiber et al. 2006; Elmegreen et al. 2007; Genzel et al. 2008; Dekel et al. 2009a; Bouché et al. 2010; Krumholz & Burkert 2010; Cacciato et al. 2012; Davé et al. 2012; Lilly et al. 2013; Saintonge et al. 2013; Dekel & Burkert 2014; Krumholz & Burkert 2016; Rathaus & Sternberg 2016; Leaman et al. 2017). In this framework, the (in)stability of the disk directly corresponds to the level of turbulence in the ISM, where turbulence is fed through external (accretion) and internal (radial flows, clump formation) events via the release of gravitational energy, creating a self-regulation cycle to maintain marginal stability (Dekel et al. 2009a; Genel et al. 2012a; but see Elmegreen & Burkert 2010).

For a snapshot in time that represents the observation of a high- z galaxy, this equilibrium situation is captured through the Toomre- Q parameter (Toomre 1964), where generally $Q < Q_{\text{crit}} \approx 1$ indicates gravitational instability. Considering the one-component approximation for a gas disk, we can write (Binney & Tremaine 2008; Escala & Larson 2008; Dekel et al. 2009b)

$$Q_{\text{gas}} = \frac{\sigma_0 \kappa}{\pi G \Sigma_{\text{gas}}} = \frac{\sigma_0}{\pi G \Sigma_{\text{gas}}} \frac{a v_c(r)}{r}. \quad (5)$$

Here, κ is the epicyclic frequency, a is a constant taking values of 1 and $\sqrt{2}$ for Keplerian and constant rotation velocity, respectively, and v_c is the circular velocity tracing the dynamical mass.

The framework of Toomre (in)stability generally refers to the linear regime, where perturbations are assumed to be axisymmetric. The galaxies studied here, however, are in the nonlinear limit where the ISM is turbulent and many stars have formed (Mandelker et al. 2014). Inoue et al. (2016) investigated the stability of simulated high- z disks, finding that large parts of the disks are in the nonlinear regime with $Q > 1$ –3. This result, however, depends on the gas fraction, which is generally too low in the simulations. Indeed, for those simulated galaxies with the highest gas fractions ($f_{\text{gas}} \sim 0.4$; still lower than for

typical $z \sim 2$ SFGs), Inoue et al. (2016) found values more compatible with observational findings. Meng et al. (2019) argued in recent work that the Toomre- Q linear stability analysis is still applicable to simulated high- z galaxies, with values of $Q \sim 0.5$ –1 in gas-rich regions (see also Behrendt et al. 2015 for simulations of isolated gas-rich disks).

Generally, for a multicomponent system, an effective Q parameter has to be computed, $Q_{\text{eff}}^{-1} = \sum_i Q_i^{-1}$, where i refers to, e.g., stars or different gas phases (e.g., Wang & Silk 1994; Escala & Larson 2008; Genzel et al. 2011; Romeo & Falstad 2013; Obreschkow et al. 2015, and references therein). Simulations of galaxy formation support a picture where $Q_{\text{eff}} \sim 1$ for high- z galaxies, and $Q_{\text{eff}} \sim 2$ –3 for low- z galaxies where the increasing impact of a stellar disk increases Q_{crit} (Hohl 1971; Athanassoula & Sellwood 1986; Bottema 2003; Immeli et al. 2004a; Kim & Ostriker 2007; Agertz et al. 2009a, 2009b; Aumer et al. 2010; Ceverino et al. 2010; Hopkins et al. 2011; Genel et al. 2012b; Danovich et al. 2015). For gas-rich, thick or clumpy disks Q_{crit} decreases instead, such that for $z \gtrsim 1$ galaxies, values of $Q_{\text{crit}} \approx 0.7$ are expected (e.g., Goldreich & Lynden-Bell 1965; Kim & Ostriker 2007; Wang et al. 2010; Romeo & Agertz 2014; Behrendt et al. 2015).

It has been shown that the gas-rich, star-forming disks observed at high redshift are at most marginally stable to gravitational fragmentation (Genzel et al. 2011; see also Swinbank et al. 2017; Johnson et al. 2018; Tadaki et al. 2018; and Fisher et al. 2017 for local high- z analogs), and Wisnioski et al. (2015) have shown that the redshift evolution predicted by Equation (5) for $Q \sim 1$ gas disks is in remarkable agreement with observations (see also, e.g., Green et al. 2014; Turner et al. 2017; White et al. 2017; Johnson et al. 2018). In addition, Genzel et al. (2011) have shown that on subkiloparsec spatially resolved scales, values of $Q \sim 0.2$ can be reached in regions of star-forming clumps, possibly demonstrating gravitational fragmentation at work.

We calculate Q_{gas} for our galaxies following Equation (5) by evaluating the circular velocity at $v_c(r = 1.38R_e)$. As mentioned in Section 3.3, this radius corresponds to the theoretical peak of a Noordermeer disk with $n_s = 1$, such that the local gradient of the rotation curve is flat, leading to $a = \sqrt{2}$. The circular velocity v_c is computed from the model rotation velocity corrected for pressure support from the turbulent motions (Burkert et al. 2010, 2016; Wuyts et al. 2016). In Figure 9, we show $f_{\text{gas}} = M_{\text{gas}}/M_{\text{bar}}$, with $M_{\text{bar}} = M_{\star} + M_{\text{gas}}$, as a function of Q_{gas} , color-coded by redshift as in Figure 4. Despite the large scatter, an anti-correlation between f_{gas} and Q_{gas} is evident, such that galaxies with higher gas fractions have lower Q (Spearman rank correlation coefficient $\rho_s = -0.30$ with significance $\sigma_\rho = 3.6$). This is in agreement with the theoretical prediction that SFGs that are more gas rich have lower Q values. The average Q_{gas} for our galaxies in the redshift bins $z \sim 0.9$; 1.5; 2.3 is $Q_{\text{gas}} = 1.2$; 0.7; 0.5 (arrows in Figure 9). Our results on the average offset of ionized versus atomic+molecular gas from Section 4.5 suggest that the cold gas tracing the bulk of the gas mass might have a velocity dispersion lower by 10–15 km^{-1} . This would lower the Q_{gas} values by a factor of ~ 1.2 –2. While our calculation of the Toomre- Q parameter is simplified through the omission of the stellar component, this suggests that thick high- z disks with high gas fractions of $\gtrsim 50\%$ can be marginally stable even down to $Q_{\text{gas}} < 0.7$.

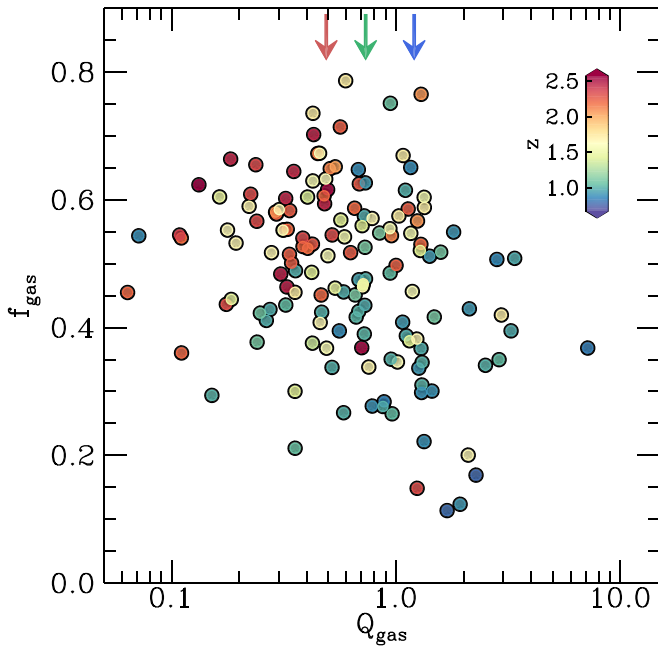


Figure 9. Gas-to-baryonic mass fraction f_{gas} as a function of Q_{gas} , color-coded by redshift. The arrows indicate the average value of Q_{gas} at $z \sim 0.9$ (blue), $z \sim 1.5$ (green), and $z \sim 2.3$ (red). f_{gas} and Q_{gas} are weakly anticorrelated with Spearman rank correlation coefficient $\rho_S = -0.30$ and significance $\sigma_\rho = 3.6$. Higher z galaxies with higher gas fractions reach values below $Q_{\text{gas}} = 1$.

5.4. Combining Feedback and Gravity

While gravitational instabilities are likely important drivers of the elevated velocity dispersions at $z > 1$, the contribution from stellar feedback-driven turbulence of the order of $10\text{--}20 \text{ km s}^{-1}$ could become comparable or even dominant for lower z , low- σ_0 galaxies. Therefore, one must consider both processes to get a complete picture.

The combination of stellar feedback and gravitational processes for turbulence driving has recently been investigated through the analytic model for structure and evolution of gas in galactic disks by Krumholz et al. (2018), who combine prescriptions for star formation, stellar feedback, and gravitational instabilities into a unified “transport+feedback” model to explain the range of observed dispersions from $z = 3$ to the present day. In their model, gas is in vertical hydrostatic equilibrium and energy equilibrium. This model assumes (isolated) rotating galactic disks built of gas and stars within a quasi-spherical dark matter halo over a wide redshift range. Disks are stable or marginally stable to gravitational collapse, regulated by mass transport through the disk. The gas is in vertical hydrostatic equilibrium, and in energy equilibrium such that losses through the decay of turbulence are balanced by energy input into the system via stellar feedback and the release of gravitational energy via mass transport through the disk.

Consistent with the discussion above, Krumholz et al. (2018) showed in their model that stellar feedback may maintain velocity dispersions of $\sim 10 \text{ km s}^{-1}$, creating a dispersion floor, while gravitational instabilities, for instance created through radial mass transport through the disk, are necessary to constantly drive velocity dispersions beyond $\sigma_0 \sim 20 \text{ km s}^{-1}$ for moderate star formation rates (see also Figure 4 by Krumholz et al. 2018). They make a prediction for galactic gas velocity dispersion and its correlation with SFR. In particular,

they show that (see their Equation (60))

$$\text{SFR} = \frac{0.42}{\pi G} \frac{1}{Q} \cdot f_{\text{gas}} v_{\text{circ}}^2 \sigma_0, \quad (6)$$

where we have substituted appropriate constants for high- z galaxies following Krumholz et al. (2018). Specifically, we adopt a rotation curve slope of $\beta = 0$, an offset between resolved and unresolved star formation law normalizations of $\phi_a = 3$, a fraction of ISM in the star-forming phase $f_{\text{sf}} = 1$, a ratio of total pressure to turbulent pressure at the midplane of $\phi_{\text{mp}} = 1.4$, a star formation efficiency per freefall time of $\epsilon_{\text{ff}} = 0.0015$, an orbital period of $t_{\text{orb,out}} = 200 \text{ Myr}$, and a maximum star formation timescale of $t_{\text{sf,max}} = 2 \text{ Gyr}$.

We make two adjustments to our data to properly compare to the model: here, and for all of Section 5.4, we subtracted 15 km s^{-1} in quadrature from our intrinsic dispersion values, denoted by $\sigma_{0,15}$, to ensure consistency with the theoretical model (see Krumholz & Burkhardt 2016 and Krumholz et al. 2018, Appendix B). This 15 km s^{-1} represents the average combination of thermal motions and expansion of H II regions that enter our ionized gas velocity dispersion measurement (see also Sections 3.4 and 4.5). We also modify our gas mass fractions: the corresponding parameter used by Krumholz et al. (2018) describes an effective gas fraction at the midplane. This has typically higher values than our gas fraction f_{gas} because of the larger stellar scale heights compared to the gas scale heights. For the comparison here, we adopt a scaling factor of 1.5 for our gas mass fractions, motivated by measurements in the solar neighborhood (McKee et al. 2015; Krumholz et al. 2018; M. Krumholz 2019, private communication).

To compare the model prediction from Equation (6) to our data, we group correlated quantities and separate the star formation properties SFR and f_{gas} from the kinematic tracers v_{circ} and σ_0 . We show the result for our kinematic sample in Figure 10, specifically the SFR divided by gas fraction as a function of circular velocity squared times intrinsic velocity dispersion. Figure 10 reveals a clear trend between the displayed quantities, with a Spearman rank correlation of $\rho_S = 0.57$ with significance $\sigma_\rho = 6.8$. We also show model predictions from Krumholz et al. (2018) as quoted in Equation (6) for three values of Q . There is a tendency for higher z galaxies to have a predicted $Q \lesssim 1$, consistent with our results presented in Figure 9. Generally, however, our galaxies scatter around $Q = 1$ at all redshifts. This suggests that SFGs self-regulate at all times such that the population of SFGs evolves roughly along lines of constant Q . This result is largely independent from the specific choices of parameters such as ϕ_a or f , which will only affect the average Q value. Note that the above correlation between SFR and velocity dispersion is predicted for both the combined “transport+feedback” model and a model without feedback, but not for models lacking the “transport” component accounting for gravitational instabilities (see also Krumholz & Burkhardt 2016).

In the following, we now investigate separately changes of circular velocity and gas fraction in the σ_0 -SFR parameter space. In Figure 11, we show for our kinematic sample the intrinsic velocity dispersion as a function of SFR, color-coded by circular velocity. As expected from the main sequence and Tully Fisher relation (Tully & Fisher 1977), which is in place for our data set at all redshifts (Übler et al. 2017), our data display a gradient such that circular velocity on average increases with increasing SFR. We plot the high- z model by

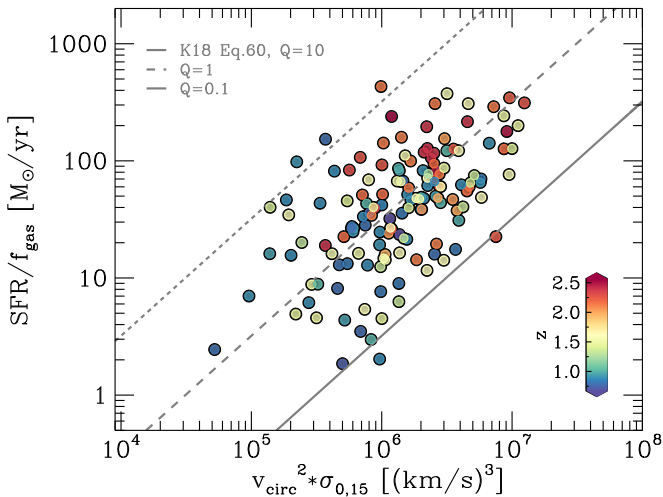


Figure 10. SFR divided by gas fraction as a function of circular velocity squared times intrinsic velocity dispersion for our kinematic sample, color-coded by redshift. The lines show predictions from the “transport+feedback high- z ” model by Krumholz et al. (2018) for different values of Q (Equation (6)). We find a strong correlation between the displayed quantities ($\rho_s = 0.57$, $\sigma_p = 6.8$), where galaxies scatter around constant Q , suggesting dominant self-regulation processes in our galaxies at all redshifts.

Krumholz et al. (2018) as lines, but we modify it such that we vary the galaxy circular velocity from $v_{\text{circ}} = 50 \text{ km s}^{-1}$ to $v_{\text{circ}} = 450 \text{ km s}^{-1}$ in order to appropriately cover the range of observed velocities in our kinematic sample. In the model framework, stellar feedback creates and sustains a dispersion floor, represented through the horizontal regime of the model lines. The predicted rapid increase of velocity dispersion with SFR, the exact location here dependent on circular velocity, requires the release of gravitational energy through radial transport through the disk (see Krumholz et al. 2018 for details). The agreement between the theoretical model and our data is remarkably good: $\sim 60\%$ of our data are matched by the model for this simple variation of only the circular velocity, with all other parameters being fixed to the fiducial “transport+feedback high- z ” parameters.

For the gas fraction, we can make only an approximate comparison. As mentioned in Section 2, gas masses for our galaxies are calculated by applying the scaling relation by Tacconi et al. (2018), since direct gas mass measurements are not available for most of our galaxies. With this, we get the total gas mass over the total baryonic mass per galaxy. Again, we use a scaling factor of 1.5 for our gas mass fractions. In Figure 12, we show the same parameter space as in Figure 11 but now color-coded by gas fraction. While galaxies with $\text{SFR} \lesssim 10 M_\odot \text{ yr}^{-1}$ have on average lower gas fractions, no strong trend is apparent at higher SFRs. We show again lines based on the “transport+feedback high- z ” model by Krumholz et al. (2018), but now we vary the gas fraction (and with it $f_{g,p}$) from $f_{g,Q} = 0.2$ to $f_{g,Q} = 1.0$ in order to explore the range of scaled gas fractions of galaxies in our kinematic sample. With solid lines, we show models with $v_\phi = 400 \text{ km s}^{-1}$, and dashed lines show $v_\phi = 200 \text{ km s}^{-1}$. It becomes clear that in the model framework, galaxies at fixed SFR and σ_0 can have higher $f_{g,Q}$ and lower v_ϕ , or lower $f_{g,Q}$ and higher v_ϕ , but rotation velocity has to be varied to cover the full range of SFRs in our observations.

Horizontal variations of the model predictions can be reached by changing the fraction of gas assumed to be in the star-forming ISM, and through changes in the outer rotation

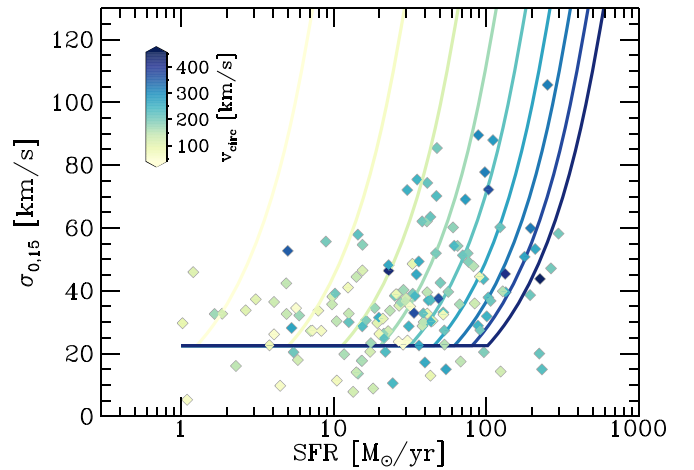


Figure 11. Intrinsic velocity dispersion $\sigma_{0,15}$ as a function of star formation rate SFR, color-coded by circular velocity. The data points show our kinematic sample. The lines are predictions from the “transport+feedback high- z ” model by Krumholz et al. (2018), where we additionally vary the galaxy circular velocity v_{circ} between 50 and 450 km s^{-1} in steps of 50 km s^{-1} . For 60% of our galaxies in the $\sigma_{0,15}$ –SFR parameter space, the model predicts the correct rotation velocity, with all other parameters being fixed as specified in the main text.

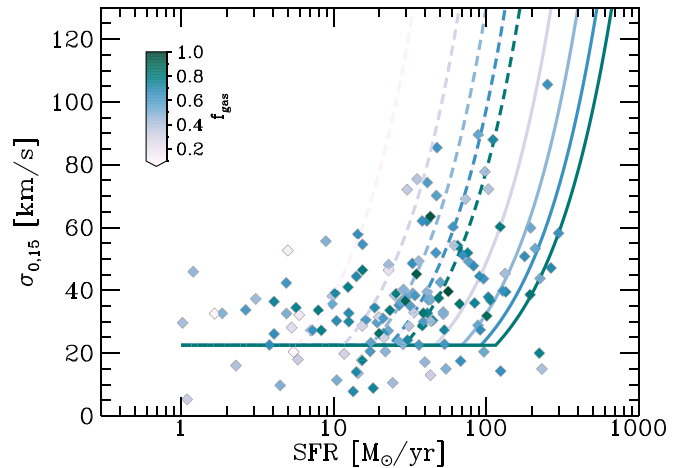


Figure 12. Intrinsic velocity dispersion $\sigma_{0,15}$ as a function of star formation rate SFR, color-coded by (scaled) gas fraction (see main text for details). The data points show our kinematic sample. The lines are predictions from the “transport+feedback high- z ” model by Krumholz et al. (2018), where we additionally vary $f_{g,Q}$ in lockstep with $f_{g,p}$ between 0.2 and 1 in steps of 0.2, and the galaxy rotation velocity v_ϕ from 200 km s^{-1} (dashed lines) to 400 km s^{-1} (solid lines). The location of the model predictions illustrate how the observed scatter in gas fractions at fixed SFR and σ_0 may be caused by different rotation velocities.

curve slope. For instance, assuming only 20% of the gas to be in the star-forming phase pushes the horizontal floor of the model below 10 km s^{-1} and lowers the predicted SFR by almost an order of magnitude. Assuming a dropping rotation curve, on the other hand, lifts the horizontal floor and increases the predicted SFR. Assuming an outer rotation curve slope of $\beta = -0.5$ increases the horizontal saturation of the model to $\sim 32 \text{ km s}^{-1}$, while increasing the star formation rate only marginally. Lang et al. (2017) have shown that the typical outer rotation curve slope of galaxies in our sample is negative. This is more pronounced at higher redshift, possibly offering an additional reason for the elevated velocity dispersions at $z \gtrsim 2$ in this model framework.

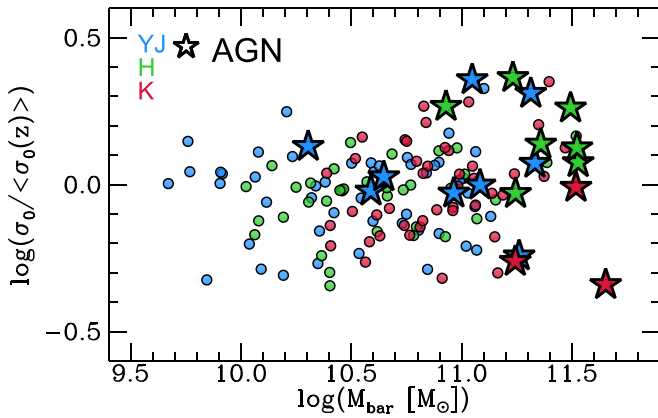


Figure 13. Redshift-normalized intrinsic velocity dispersion as a function of baryonic mass. Blue, green, and red indicate $z \sim 0.9$, $z \sim 1.5$, and $z \sim 2.3$ SFGs, respectively. Galaxies that host an AGN are shown as stars. Most galaxies with $\log(M_{\text{bar}}/M_{\odot}) \gtrsim 11.3$ have above-average velocity dispersions and about half of them host an identified AGN.

Considering these analytic model prescriptions and the typical uncertainty of the intrinsic dispersion measurements of $\delta\sigma_0 \sim 10 \text{ km s}^{-1}$ in our kinematic sample, we conclude that galaxies with $\sigma_0 \gtrsim 35 \text{ km s}^{-1}$ are dominated by gravitational instability-driven turbulence. This encompasses more than 60% of galaxies in our sample, underlining the importance of gravity-driven turbulence in SFGs at $z \sim 1-3$.

5.5. AGN Feedback

As a final remark, we briefly want to comment on AGN feedback as a potential additional source for elevated velocity dispersions in the SFGs in our kinematic sample. While we excluded galaxies, or regions of galaxies, that are so strongly affected by the AGN and associated outflows that the disk kinematics cannot be recovered, we do not entirely exclude AGNs. This ensures that we can explore the full mass range covered by the KMOS^{3D} survey, including the high-mass end where at $\log(M_*/M_{\odot}) > 11$, above the Schechter mass, the fraction of AGNs increases rapidly (Förster Schreiber et al. 2014, 2018; Genzel et al. 2014).

While we do not find significant correlations between z -normalized σ_0 and mass properties (Table 7), we do note a cloud of galaxies from all redshifts with dispersions above average for the highest stellar ($\log(M_*/M_{\odot}) > 11$) and baryonic masses ($\log(M_{\text{bar}}/M_{\odot}) \gtrsim 11.3$) as shown in Figure 13. About half of the $\log(M_{\text{bar}}/M_{\odot}) \gtrsim 11.3$ above-average dispersion galaxies are known to host an AGN (stars in Figure 13). We speculate that the energy deposited by strong AGN feedback in the form of nuclear outflows could induce turbulence in the disk via the reaccretion of material at larger radii.

It is important to keep in mind that outflow components with velocities similar to the galaxy rotation velocity can broaden the line width but may not be distinguishable from the star-forming regions, due to S/N limitations. Comparing to the deep AO data from the SINS/zC-SINF survey that we show in Figure 8, one of the three identified $\log(M_*/M_{\odot}) \gtrsim 11$ AGN (Q2343-BX610), shows above-average velocity dispersions (after excluding the regions clearly affected by the nuclear outflow), while the other two (D3a-6004, D3a-15504) have average dispersions.

6. Conclusions

We have investigated the evolution of the ionized gas intrinsic velocity dispersions, σ_0 , between $0.6 < z < 2.6$ based on data from our full KMOS^{3D} survey. We have selected a high-quality, rotation-dominated ($v_{\text{rot}}/\sigma_0 \geq 1$) sample for which we forward-modeled in a Bayesian framework the one-dimensional galaxy kinematics extracted from the H α velocity and velocity dispersion maps, taking into account instrumental effects, beam-smearing, and pressure support. Our main conclusions are as follows:

1. Assuming an isotropic and radially constant intrinsic velocity dispersion, we find an average decrease of the H α intrinsic dispersion for our kinematic sample from $\sigma_0 \sim 46 \text{ km s}^{-1}$ at $z \sim 2.3$ to $\sigma_0 \sim 31 \text{ km s}^{-1}$ at $z \sim 0.9$, solidifying trends previously reported in the literature (Section 4.1). Putting our sample into the broader context of literature measurements from $z = 4$ to $z = 0$, tracing ionized, molecular, and atomic gas phases, confirms the general increase of intrinsic galaxy velocity dispersion with redshift (Section 4.4).
2. Comparing the redshift evolution of ionized and molecular plus atomic gas velocity dispersion, we find that the ionized gas dispersion is on average higher by $\sim 12 \text{ km s}^{-1}$ (Section 4.5). This offset can in principle be accounted for through the different gas temperatures together with the line broadening through the expansion of the H II regions the ionized gas emission typically originates from.
3. For our KMOS^{3D} kinematic sample, we find that there is intrinsic scatter in the σ_0 distribution at fixed redshift after accounting for measurement and modeling uncertainties, and it increases for our highest redshift slice (Section 4.2). However, we cannot single out a physical mechanism behind this scatter. This could imply that the velocity dispersion is highly variable in time, due to a dynamic mechanism such as minor mergers or variation in accretion (see Hung et al. 2019 for evidence from simulations). Alternatively, the scatter could be caused by the interplay of different physical properties responsible for maintaining marginal stability (see Section 5.4).
4. Investigating the physical driver of the elevated velocity dispersions at higher redshift, we find that galaxies in our kinematic sample are at most marginally Toomre-stable, i.e., they are consistent with their turbulence being powered through gravitational instabilities in a self-regulated environment (Sections 5.3 and 5.4).
5. We find no evidence from our high-resolution SINS/zC-SINF AO data that stellar feedback as traced through Σ_{SFR} typically increases the velocity dispersion on subgalactic scales beyond the average level, or that the local velocity dispersion correlates strongly with Σ_{SFR} , suggesting that contributions from stellar feedback to turbulence driving are minor for our $z > 1$ SFGs (Section 5.2).
6. We find good agreement between data from our KMOS^{3D} kinematic sample and predictions from the state-of-the-art analytical model of galaxy formation and evolution by Krumholz et al. (2018), further strengthening the evidence that the majority of our galaxies ($\gtrsim 60\%$) are dominated by gravity-driven turbulence (Section 5.4).

The measurement of intrinsic gas velocity dispersion at $z > 0$ is challenging. Next-generation instruments such as ERIS+AO at the VLT or HARMONI at the ELT will expand current samples on spatial scales that are currently only achievable for strongly lensed objects, and push spectral scales down to $\sim 15 \text{ km s}^{-1}$. The statistics from these observations will facilitate further investigation of the scatter of the intrinsic velocity dispersion at fixed redshift, and tests of theoretical predictions such as the transition regime from gravity-driven turbulence to feedback-driven turbulence as a function of redshift and mass (Krumholz et al. 2018). Deep, high-S/N observations of particularly molecular gas reaching 1–2 kpc resolution at $z > 1$ with NOEMA or ALMA are necessary to test if the redshift evolution of molecular and ionized gas velocity dispersion is indeed comparable.

We are grateful to the anonymous referee for a very constructive report that helped to improve the quality of this manuscript. We thank the ESO Paranal staff for their helpful support with the KMOS observations for this work. We are grateful to Raymond Simons and Susan Kassin for providing us with data from the DEEP2 and SIGMA surveys. We thank

Luca Cortese, Amiel Sternberg, Vadim Semenov, and Chia-Yu Hu for fruitful discussions, and we are particularly grateful to Blakesley Burkhart, Mark Krumholz, and Andreas Schruba for valuable comments on various aspects of this work. D.W. acknowledges the support of the Deutsche Forschungsgemeinschaft via projects WI 3871/1-1 and WI 3871/1-2. E.W. acknowledges support by the Australian Research Council Centre of Excellence for All Sky Astrophysics in 3 Dimensions (ASTRO 3D), through project number CE170100013. M.F. acknowledges the support from the European Research Council (ERC) under the European Union’s Horizon 2020 research and innovation programme (grant agreement No. 757535). P.L. acknowledges funding from the ERC under the European Union’s Horizon 2020 research and innovation programme (grant agreement No. 694343).

Appendix A Example Galaxies and Fits

We show examples of galaxies in our kinematic sample together with their best-fit kinematic models in Figure 14. See the figure caption for details.

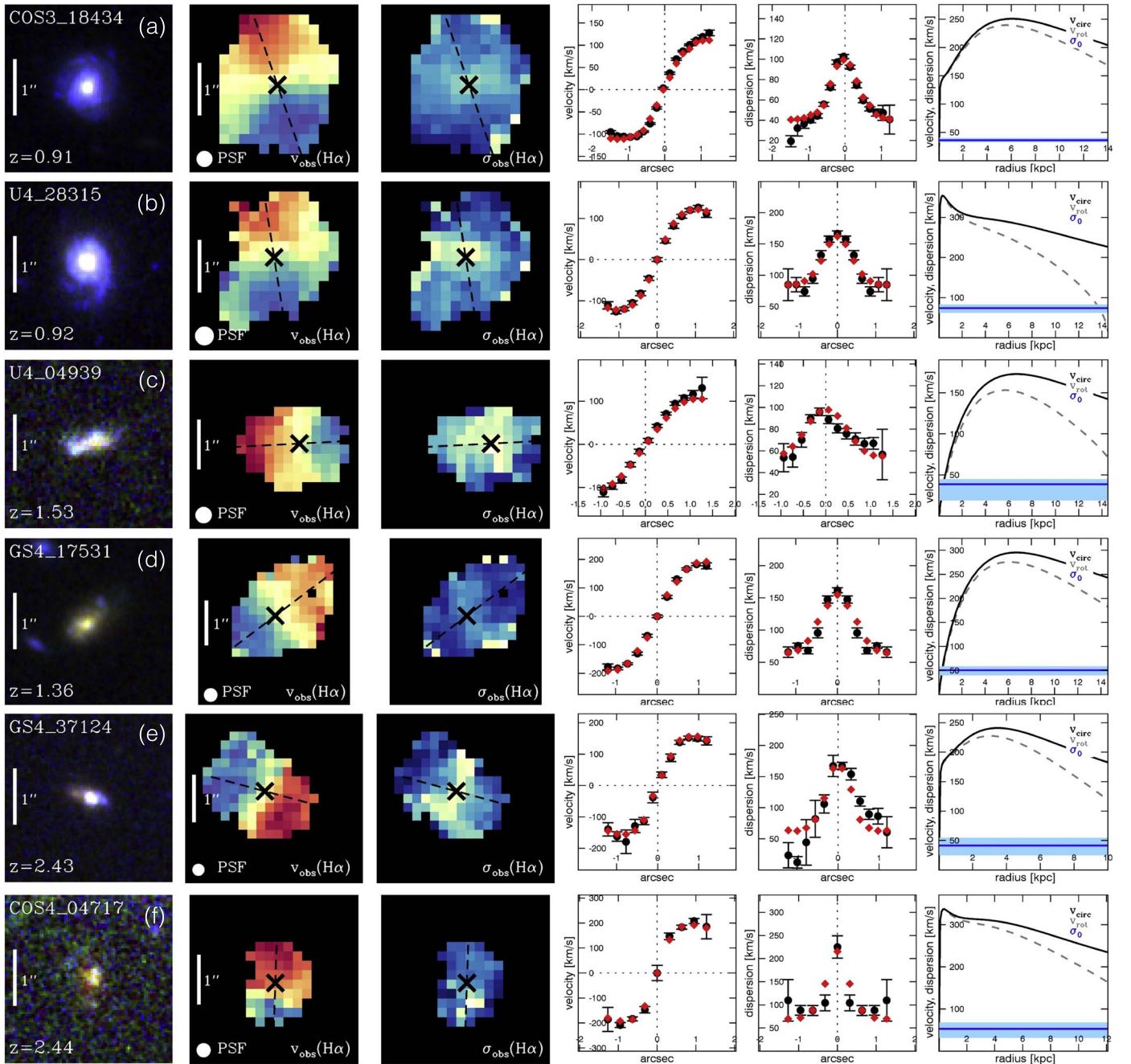


Figure 14. Example cases of galaxies in our kinematic sample. From top to bottom, we show for each redshift slice a galaxy modeled with setup 1 and with setup 2 (see Section 3.2). From left to right, we show an *IJH HST* color-composite image; the projected $H\alpha$ velocity map; the projected $H\alpha$ velocity dispersion map; the observed velocity $v_{\text{rot}}(r) \cdot \sin(i)$ along the kinematic major axis (black) and the best-fit model (red); the corresponding observed velocity dispersion $\sigma(r)$; and the intrinsic model circular velocity v_{circ} (black), rotation velocity v_{rot} (gray dashed), and intrinsic velocity dispersion (blue) together with its uncertainties derived from the MCMC posterior distribution (blue shading). The kinematic maps and profiles are corrected for the instrument line-spread function, but not for beam-smearing. The kinematic major axis is indicated by the black dashed line on top of the velocity and dispersion maps, and the black crosses indicate the midpoint between the observed minimum and maximum velocities (not necessarily the kinematic center). Note that the intrinsic rotation curves are falling by construction because we do not include a dark matter halo (but see Section 3.2). Rows (a), (c), and (e) show examples from setup 1, and rows (b), (d), and (f) show examples from setup 2.

Appendix B

Alternative Fits to Our KMOS^{3D} Velocity Dispersions

We list fits to our KMOS^{3D} velocity dispersion data from $z = 2.6$ to $z = 0.6$ in $\sigma_0 - \log(1+z)$ space and

$\log(\sigma_0) - \log(1+z)$ space in Tables 8 and 9, respectively. These results agree with our fiducial fits in $\sigma_0 - z$ space listed in Table 3, and do not change our conclusions.

Table 8

Results from the Linear Regression Fits of the Form $\sigma_0/\text{km s} = a + b \cdot \log(1 + z) + c$ for our Kinematic Sample, where a and b are the Regression Coefficients, and c is the Intrinsic Random Scatter about the Regression (See Kelly 2007)

Sample	N	a	b	σ_c	l_{corr}	σ_0 at $z \sim 0.9$ (km s^{-1})	σ_0 at $z \sim 1.5$ (km s^{-1})	σ_0 at $z \sim 2.3$ (km s^{-1})
Including Upper Limits	175	19.4 ± 3.8	52.6 ± 10.1	9.8 ± 1.1	0.48 ± 0.08	33.8	40.6	46.5
Excluding Upper Limits (Robust)	147	19.5 ± 4.5	53.1 ± 11.4	10.4 ± 1.1	0.46 ± 0.09	34.1	40.9	46.9
Using Formal Best-fit σ_0	175	19.5 ± 4.5	53.1 ± 11.3	10.4 ± 1.1	0.46 ± 0.09	34.1	40.9	46.8

Note. For each parameter a and b , the standard deviation of c , and the derived linear correlation coefficient l_{corr} between σ_0 and z , we list the median together with the standard deviation of the posterior distribution. For each redshift slice, we list the best-fit σ_0 value corresponding to these medians.

Table 9

Results from the Linear Regression Fits of the Form $\log(\sigma_0/\text{km s}) = a + b \cdot \log(1 + z) + c$ for our Kinematic Sample, where a and b are the Regression Coefficients, and c is the Intrinsic Random Scatter about the Regression (See Kelly 2007)

Sample	N	a	b	σ_c	l_{corr}	σ_0 at $z \sim 0.9$ (km s^{-1})	σ_0 at $z \sim 1.5$ (km s^{-1})	σ_0 at $z \sim 2.3$ (km s^{-1})
Including Upper Limits	175	1.29 ± 0.05	0.77 ± 0.13	0.12 ± 0.01	0.54 ± 0.08	31.8	39.9	48.6
Excluding Upper Limits (Robust)	147	1.38 ± 0.05	0.61 ± 0.13	0.11 ± 0.01	0.49 ± 0.09	35.3	42.2	49.4
Using Formal Best-fit σ_0	175	1.30 ± 0.05	0.75 ± 0.13	0.12 ± 0.01	0.53 ± 0.07	32.3	40.3	49.0

Note. For each parameter a and b , the standard deviation of c , and the derived linear correlation coefficient l_{corr} between σ_0 and z , we list the median together with the standard deviation of the posterior distribution. For each redshift slice, we list the best-fit σ_0 value corresponding to these medians.

Appendix C

Correlations of Physical Properties with Velocity Dispersion and Redshift-normalized Velocity Dispersion

We show correlations of various physical properties with velocity dispersion after (see Equation (2)) and before correcting for the redshift dependence of σ_0 in Figures 15

and 16 (see also Table 7). While several properties positively correlate with σ_0 , particularly SFR and M_{gas} , we do not find any significant correlation after correcting for the redshift dependence of σ_0 . This means that we cannot readily identify a single physical driving source behind the intrinsic scatter in σ_0 (see discussions in Sections 4.2 and 5).

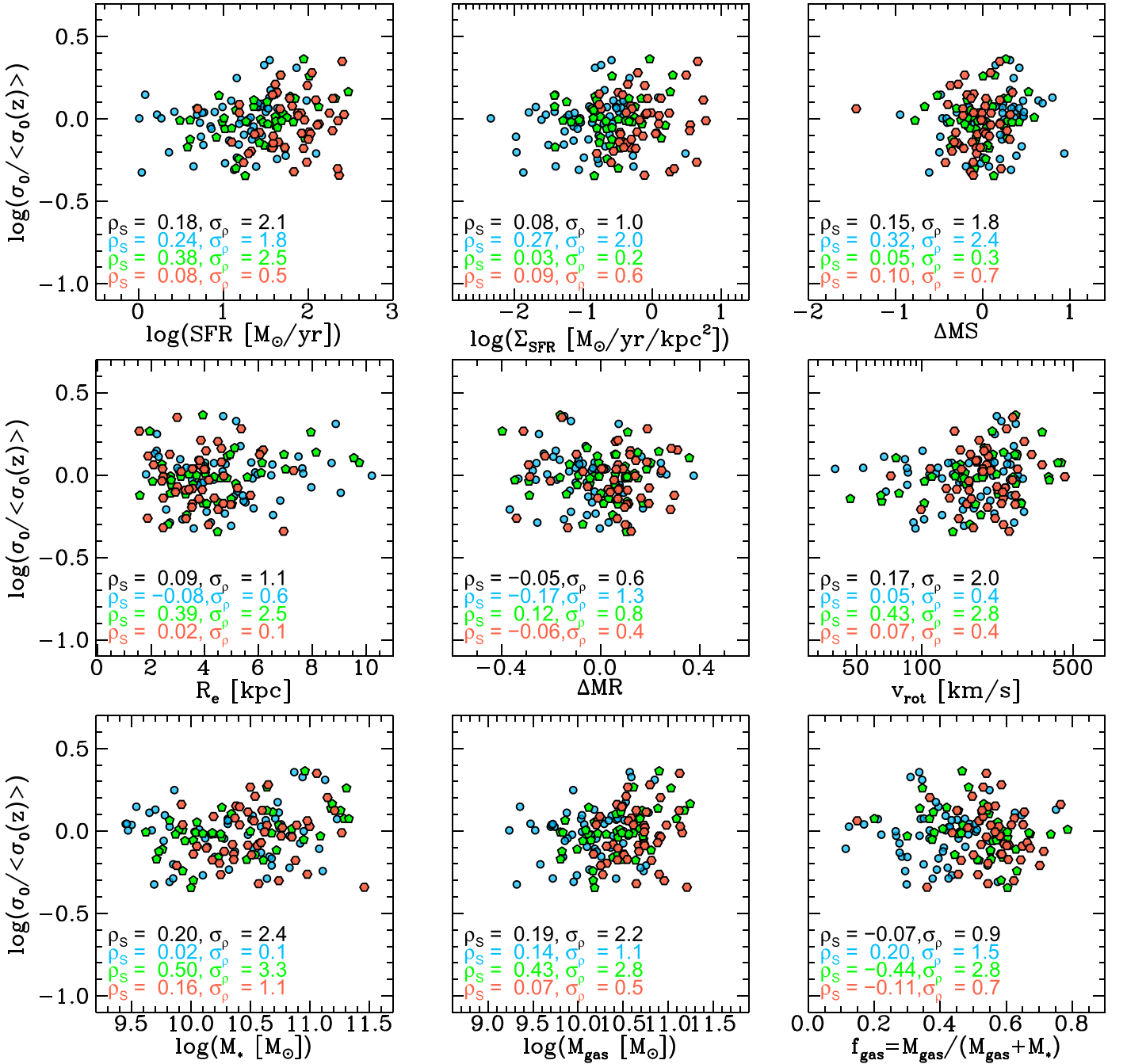


Figure 15. Redshift-normalized velocity dispersion (see Equation (2)) as a function of several physical properties. Colors show our redshift subsamples at $z \sim 0.9$ (blue), $z \sim 1.5$ (green), and $z \sim 2.3$ (red). Spearman rank correlation coefficients ρ_s and their significance σ_p are listed in each panel for the full sample (black) and the individual redshift bins (colors). We do not find any significant correlations between redshift-normalized velocity dispersion and the considered physical properties (see Table 7 for additional quantities) for our kinematic KMOS^{3D} sample, meaning that we cannot identify a single physical driving source behind the intrinsic scatter in velocity dispersion.

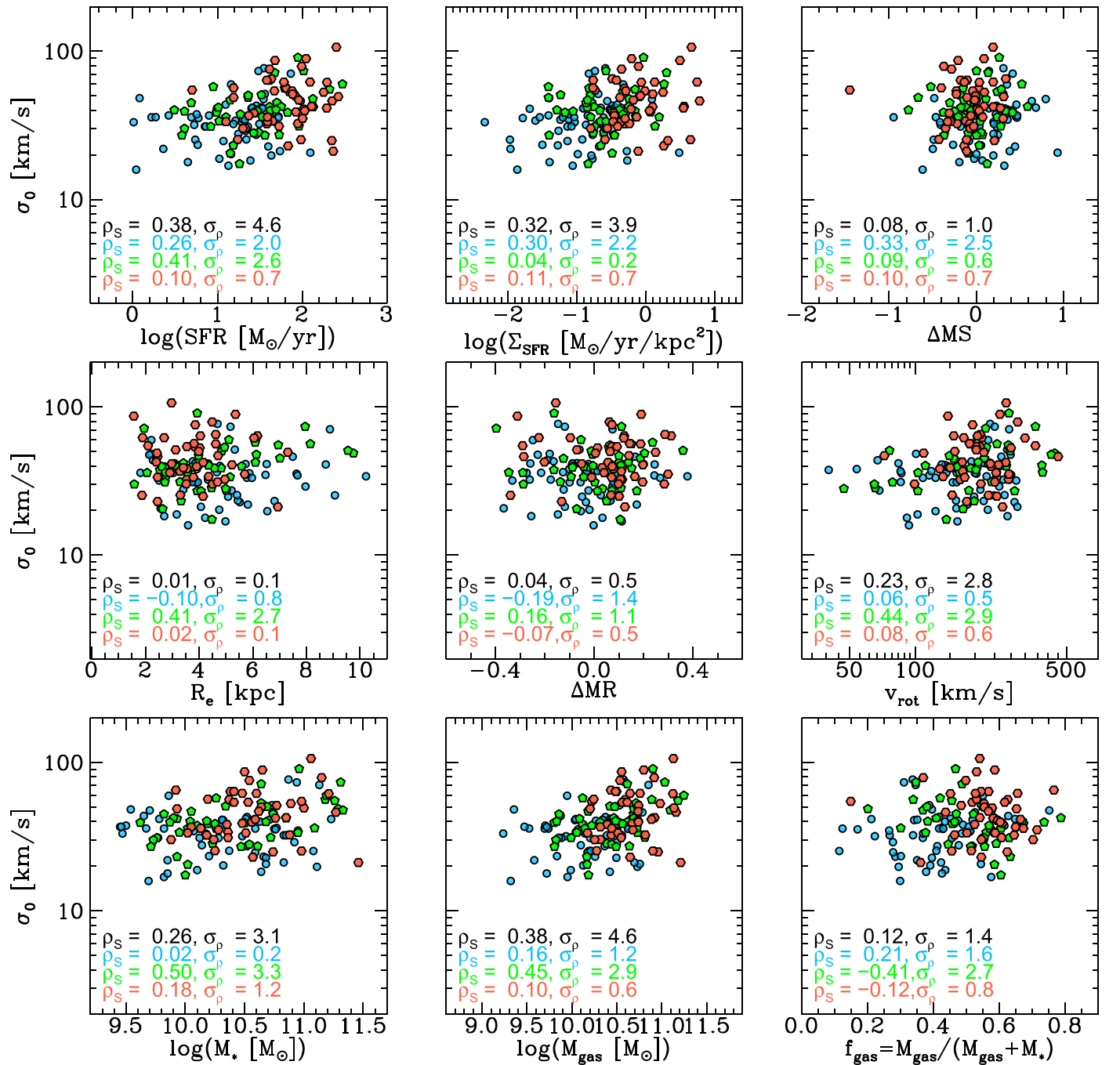


Figure 16. Velocity dispersion as a function of several physical properties. Colors show our redshift subsamples at $z \sim 0.9$ (blue), $z \sim 1.5$ (green), and $z \sim 2.3$ (red). Spearman rank correlation coefficients ρ_S and their significance σ_p are listed in each panel for the full sample (black) and the individual redshift bins (colors). Velocity dispersion positively correlates with several physical properties, some of which correlate themselves with redshift. For our kinematic KMOS^{3D} sample, we find the strongest and most significant correlations between σ_0 and SFR, as well as M_{gas} , which we further investigate in Section 5.

ORCID iDs

H. Übler <https://orcid.org/0000-0003-4891-0794>
 R. Genzel <https://orcid.org/0000-0002-2767-9653>
 N. M. Förster Schreiber <https://orcid.org/0000-0003-4264-3381>
 T. T. Shimizu <https://orcid.org/0000-0002-2125-4670>
 S. H. Price <https://orcid.org/0000-0002-0108-4176>
 L. J. Tacconi <https://orcid.org/0000-0002-1485-9401>
 S. Belli <https://orcid.org/0000-0002-5615-6018>
 D. J. Wilman <https://orcid.org/0000-0002-1822-4462>
 M. Fossati <https://orcid.org/0000-0002-9043-8764>

R. L. Davies <https://orcid.org/0000-0002-3324-4824>
 A. Beifiori <https://orcid.org/0000-0001-8017-6097>
 R. Bender <https://orcid.org/0000-0001-7179-0626>
 G. B. Brammer <https://orcid.org/0000-0003-2680-005X>
 A. Burkert <https://orcid.org/0000-0001-6879-9822>
 R. Herrera-Camus <https://orcid.org/0000-0002-2775-0595>
 P. Lang <https://orcid.org/0000-0002-5681-3575>
 D. Lutz <https://orcid.org/0000-0003-0291-9582>
 I. G. Momcheva <https://orcid.org/0000-0003-1665-2073>
 T. Naab <https://orcid.org/0000-0002-7314-2558>
 E. J. Nelson <https://orcid.org/0000-0002-7524-374X>

R. P. Saglia  <https://orcid.org/0000-0003-0378-7032>
 K. Tadaki  <https://orcid.org/0000-0001-9728-8909>
 P. G. van Dokkum  <https://orcid.org/0000-0002-8282-9888>
 S. Wuyts  <https://orcid.org/0000-0003-3735-1931>

References

- Agertz, O., Lake, G., Teyssier, R., et al. 2009a, *MNRAS*, 392, 294
 Agertz, O., Teyssier, R., & Moore, B. 2009b, *MNRAS*, 397, L64
 Athanassoula, E., & Sellwood, J. A. 1986, *MNRAS*, 221, 213
 Aumer, M., & Binney, J. 2017, *MNRAS*, 470, 2113
 Aumer, M., Binney, J., & Schönrich, R. 2016, *MNRAS*, 462, 1697
 Aumer, M., Burkert, A., Johansson, P. H., & Genzel, R. 2010, *ApJ*, 719, 1230
 Baumgartner, V., & Breitschwerdt, D. 2013, *A&A*, 557, A140
 Behrendt, M., Burkert, A., & Schartmann, M. 2015, *MNRAS*, 448, 1007
 Binney, J., & Tremaine, S. 2008, *Galactic Dynamics* (2nd ed.; Princeton, NJ: Princeton Univ. Press)
 Bolatto, A. D., Wong, T., Utomo, D., et al. 2017, *ApJ*, 846, 159
 Bottema, R. 2003, *MNRAS*, 344, 358
 Bouché, N., Dekel, A., Genzel, R., et al. 2010, *ApJ*, 718, 1001
 Boulanger, F., & Viallefond, F. 1992, *A&A*, 266, 37
 Bovy, J., Rix, H.-W., Liu, C., et al. 2012, *ApJ*, 753, 148
 Bovy, J., Rix, H.-W., Schlafly, E. F., et al. 2016, *ApJ*, 823, 30
 Brammer, G. B., van Dokkum, P. G., Franx, M., et al. 2012, *ApJS*, 200, 13
 Brammer, G. B., Whitaker, K. E., van Dokkum, P. G., et al. 2011, *ApJ*, 739, 24
 Brunt, C. M., Heyer, M. H., & Mac Low, M. M. 2009, *A&A*, 504, 883
 Bruzual, G., & Charlot, S. 2003, *MNRAS*, 344, 1000
 Burkert, A., Förster Schreiber, N. M., Genzel, R., et al. 2016, *ApJ*, 826, 214
 Burkert, A., Genzel, R., Bouché, N., et al. 2010, *ApJ*, 725, 2324
 Burkert, A., Truran, J. W., & Hensler, G. 1992, *ApJ*, 391, 651
 Cacciato, M., Dekel, A., & Genel, S. 2012, *MNRAS*, 421, 818
 Caldu-Primo, A., & Schruha, A. 2016, *AJ*, 151, 34
 Caldu-Primo, A., Schruha, A., Walter, F., et al. 2013, *AJ*, 146, 150
 Calzetti, D., Armus, L., Bohlin, R. C., et al. 2000, *ApJ*, 533, 682
 Cappellari, M., Scott, N., Alatalo, K., et al. 2013, *MNRAS*, 432, 1709
 Ceverino, D., Dekel, A., & Bournaud, F. 2010, *MNRAS*, 404, 2151
 Chabrier, G. 2003, *PASP*, 115, 763
 Contini, T., Garilli, B., Le Fèvre, O., et al. 2012, *A&A*, 539, A91
 Cortese, L., Catinella, B., & Janowiecki, S. 2017, *ApJ*, 848, L7
 Cresci, G., Hicks, E. K. S., Genzel, R., et al. 2009, *ApJ*, 697, 115
 Dalcanton, J. J., & Bernstein, R. A. 2002, *AJ*, 124, 1328
 Danovich, M., Dekel, A., Hahn, O., Ceverino, D., & Primack, J. 2015, *MNRAS*, 449, 2087
 Davé, R., Finlator, K., & Oppenheimer, B. D. 2012, *MNRAS*, 421, 98
 Davies, R., Förster Schreiber, N. M., Cresci, G., et al. 2011, *ApJ*, 741, 69
 Davies, R. I., Maciejewski, W., Hicks, E. K. S., et al. 2009, *ApJ*, 702, 114
 Davis, M., Faber, S. M., Newman, J., et al. 2003, *Proc. SPIE*, 4834, 161
 Dekel, A., Birnboim, Y., Engel, G., et al. 2009a, *Natur*, 457, 451
 Dekel, A., & Burkert, A. 2014, *MNRAS*, 438, 1870
 Dekel, A., Sari, R., & Ceverino, D. 2009b, *ApJ*, 703, 785
 Di Teodoro, E. M., Fraternali, F., & Miller, S. H. 2016, *A&A*, 594, A77
 Dib, S., Bell, E., & Burkert, A. 2006, *ApJ*, 638, 797
 Dickey, J. M., Hanson, M. M., & Helou, G. 1990, *ApJ*, 352, 522
 Druard, C., Braine, J., Schuster, K. F., et al. 2014, *A&A*, 567, A118
 Dutton, A. A., & Macciò, A. V. 2014, *MNRAS*, 441, 3359
 Elmegreen, B. G., & Burkert, A. 2010, *ApJ*, 712, 294
 Elmegreen, B. G., & Elmegreen, D. M. 2006, *ApJ*, 650, 644
 Elmegreen, B. G., & Scalo, J. 2004, *ARA&A*, 42, 211
 Elmegreen, D. M., Elmegreen, B. G., Ravindranath, S., & Coe, D. A. 2007, *ApJ*, 658, 763
 Epinat, B., Amram, P., Balkowski, C., & Marcelin, M. 2010, *MNRAS*, 401, 2113
 Epinat, B., Amram, P., & Marcelin, M. 2008, *MNRAS*, 390, 466
 Epinat, B., Contini, T., Le Fèvre, O., et al. 2009, *A&A*, 504, 789
 Epinat, B., Tasca, L., Amram, P., et al. 2012, *A&A*, 539, A92
 Escala, A., & Larson, R. B. 2008, *ApJL*, 685, L31
 Fisher, D. B., Bolatto, A. D., White, H., et al. 2019, *ApJ*, 870, 46
 Fisher, D. B., Glazebrook, K., Abraham, R. G., et al. 2017, *ApJL*, 839, L5
 Förster Schreiber, N. M., Genzel, R., Bouché, N., et al. 2009, *ApJ*, 706, 1364
 Förster Schreiber, N. M., Genzel, R., Lehnert, M. D., et al. 2006, *ApJ*, 645, 1062
 Förster Schreiber, N. M., Genzel, R., Newman, S. F., et al. 2014, *ApJ*, 787, 38
 Förster Schreiber, N. M., Renzini, A., Mancini, C., et al. 2018, *ApJS*, 238, 21
 Freundlich, J., Combes, F., Tacconi, L. J., et al. 2019, *A&A*, 622, A105
 Fukui, Y., Kawamura, A., Wong, T., et al. 2009, *ApJ*, 705, 144
 Gatto, A., Walch, S., Low, M. M. M., et al. 2015, *MNRAS*, 449, 1057
 Genel, S., Dekel, A., & Cacciato, M. 2012a, *MNRAS*, 425, 788
 Genel, S., Naab, T., Genzel, R., et al. 2012b, *ApJ*, 745, 11
 Genzel, R., Burkert, A., Bouché, N., et al. 2008, *ApJ*, 687, 59
 Genzel, R., Förster Schreiber, N. M., Lang, P., et al. 2014, *ApJ*, 785, 75
 Genzel, R., Förster Schreiber, N. M., Übler, H., et al. 2017, *Natur*, 543, 397
 Genzel, R., Newman, S., Jones, T., et al. 2011, *ApJ*, 733, 101
 Genzel, R., Tacconi, L. J., Eisenhauer, F., et al. 2006, *Natur*, 442, 786
 Genzel, R., Tacconi, L. J., Kurk, J., et al. 2013, *ApJ*, 773, 68
 Gilmore, G., & Reid, N. 1983, *MNRAS*, 202, 1025
 Girard, M., Dessauges-Zavadsky, M., Schaerer, D., et al. 2018, *A&A*, 613, A72
 Glazebrook, K. 2013, *PASA*, 30, e056
 Gnerucci, A., Marconi, A., Cresci, G., et al. 2011, *A&A*, 528, A88
 Goldreich, P., & Lynden-Bell, D. 1965, *MNRAS*, 130, 97
 Grand, R. J. J., Springel, V., Gómez, F. A., et al. 2016, *MNRAS*, 459, 199
 Green, A. W., Glazebrook, K., McGregor, P. J., et al. 2010, *Natur*, 467, 684
 Green, A. W., Glazebrook, K., McGregor, P. J., et al. 2014, *MNRAS*, 437, 1070
 Grogin, N. A., Kocevski, D. D., Faber, S. M., et al. 2011, *ApJS*, 197, 35
 Heyer, M., & Dame, T. M. 2015, *ARA&A*, 53, 583
 Heyer, M. H., & Brunt, C. M. 2004, *ApJL*, 615, L45
 Hohl, F. 1971, *ApJ*, 168, 343
 Hopkins, P. F., Quataert, E., & Murray, N. 2011, *MNRAS*, 417, 950
 Hung, C.-L., Hayward, C. C., Yuan, T., et al. 2019, *MNRAS*, 482, 5125
 Ianjamasimanana, R., de Blok, W. J. G., Walter, F., et al. 2015, *AJ*, 150, 47
 Ianjamasimanana, R., de Blok, W. J. G., Walter, F., & Heald, G. H. 2012, *AJ*, 144, 96
 Immeli, A., Samland, M., Gerhard, O., & Westera, P. 2004a, *A&A*, 413, 547
 Immeli, A., Samland, M., Westera, P., & Gerhard, O. 2004b, *ApJ*, 611, 20
 Inoue, S., Dekel, A., Mandelker, N., et al. 2016, *MNRAS*, 456, 2052
 Johnson, H. L., Harrison, C. M., Swinbank, A. M., et al. 2018, *MNRAS*, 474, 5076
 Jones, T. A., Swinbank, A. M., Ellis, R. S., Richard, J., & Stark, D. P. 2010, *MNRAS*, 404, 1247
 Jung, M. R., Mac Low, M.-M., & Bryan, G. L. 2009, *ApJ*, 704, 137
 Jurić, M., Ivezić, Ž., Brooks, A., et al. 2008, *ApJ*, 673, 864
 Kamphuis, J., & Sancisi, R. 1993, *A&A*, 273, L31
 Kassin, S. A., Weiner, B. J., Faber, S. M., et al. 2007, *ApJL*, 660, L35
 Kassin, S. A., Weiner, B. J., Faber, S. M., et al. 2012, *ApJ*, 758, 106
 Kelly, B. C. 2007, *ApJ*, 665, 1489
 Kim, C.-G., & Ostriker, E. C. 2018, *ApJ*, 853, 173
 Kim, C.-G., Ostriker, E. C., & Kim, W.-T. 2013, *ApJ*, 776, 1
 Kim, W.-T., & Ostriker, E. C. 2007, *ApJ*, 660, 1232
 Koch, E. W., Rosolowsky, E. W., Schruha, A., et al. 2019, *MNRAS*, 485, 2324
 Koekemoer, A. M., Faber, S. M., Ferguson, H. C., et al. 2011, *ApJS*, 197, 36
 Kriek, M., Shapley, A. E., Reddy, N. A., et al. 2015, *ApJS*, 218, 15
 Krumholz, M., & Burkert, A. 2010, *ApJ*, 724, 895
 Krumholz, M. R., & Burkert, B. 2016, *MNRAS*, 458, 1671
 Krumholz, M. R., Burkert, B., Forbes, J. C., & Crocker, R. M. 2018, *MNRAS*, 477, 2716
 Labbé, I., Rudnick, G., Franx, M., et al. 2003, *ApJL*, 591, L95
 Lang, P., Förster Schreiber, N. M., Genzel, R., et al. 2017, *ApJ*, 840, 92
 Lang, P., Wuyts, S., Somerville, R. S., et al. 2014, *ApJ*, 788, 11
 Larson, R. B. 1981, *MNRAS*, 194, 809
 Law, D. R., Steidel, C. C., Erb, D. K., et al. 2009, *ApJ*, 697, 2057
 Leaman, R., Mendel, J. T., Wisnioski, E., et al. 2017, *MNRAS*, 472, 1879
 Lehnert, M. D., Le Tiran, L., Nesvadba, N. P. H., et al. 2013, *A&A*, 555, A72
 Lehnert, M. D., Nesvadba, N. P. H., Le Tiran, L., et al. 2009, *ApJ*, 699, 1660
 Leroy, A. K., Walter, F., Bigiel, F., et al. 2009, *AJ*, 137, 4670
 Leroy, A. K., Walter, F., Brinks, E., et al. 2008, *AJ*, 136, 2782
 Levy, R. C., Bolatto, A. D., Teuben, P., et al. 2018, *ApJ*, 860, 92
 Lilly, S. J., Carollo, C. M., Pipino, A., Renzini, A., & Peng, Y. 2013, *ApJ*, 772, 119
 Livermore, R. C., Jones, T. A., Richard, J., et al. 2015, *MNRAS*, 450, 1812
 Lutz, D., Poglitsch, A., Altieri, B., et al. 2011, *A&A*, 532, A90
 Mac Low, M.-M., & Klessen, R. S. 2004, *RvMP*, 76, 125
 Mac Low, M.-M., Klessen, R. S., Burkert, A., & Smith, M. D. 1998, *PhRvL*, 80, 2754
 Mac Low, M.-M., McCray, R., & Norman, M. L. 1989, *ApJ*, 337, 141
 Magnelli, B., Popesso, P., Berta, S., et al. 2013, *A&A*, 553, A132
 Mandelker, N., Dekel, A., Ceverino, D., et al. 2014, *MNRAS*, 443, 3675
 Mason, C. A., Treu, T., Fontana, A., et al. 2017, *ApJ*, 838, 14
 McKee, C. F., & Ostriker, E. C. 2007, *ARA&A*, 45, 565
 McKee, C. F., Parravano, A., & Hollenbach, D. J. 2015, *ApJ*, 814, 13

- Meng, X., Gnedin, O., & Li, H. 2019, *MNRAS*, **486**, 1574
- Meurer, G. R., Carignan, C., Beaulieu, S. F., & Freeman, K. C. 1996, *AJ*, **111**, 1551
- Miller, S. H., Ellis, R. S., Sullivan, M., et al. 2012, *ApJ*, **753**, 74
- Mogotsi, K. M., de Blok, W. J. G., Caldú-Primo, A., et al. 2016, *AJ*, **151**, 15
- Moiseev, A. V., Tikhonov, A. V., & Klypin, A. 2015, *MNRAS*, **449**, 3568
- Momcheva, I. G., Brammer, G. B., van Dokkum, P. G., et al. 2016, *ApJS*, **225**, 27
- Moster, B. P., Naab, T., & White, S. D. M. 2018, *MNRAS*, **477**, 1822
- Naab, T., & Ostriker, J. P. 2017, *ARA&A*, **55**, 59
- Navarro, J. F., Frenk, C. S., & White, S. D. M. 1996, *ApJ*, **462**, 563
- Nelson, E. J., van Dokkum, P. G., Förster Schreiber, N. M., et al. 2016, *ApJ*, **828**, 27
- Newman, S. F., Genzel, R., Förster Schreiber, N. M., et al. 2013, *ApJ*, **767**, 104
- Noguchi, M. 1999, *ApJ*, **514**, 77
- Noordermeer, E. 2008, *MNRAS*, **385**, 1359
- Obreschkow, D., Glazebrook, K., Bassett, R., et al. 2015, *ApJ*, **815**, 97
- Ostriker, E. C., & Shetty, R. 2011, *ApJ*, **731**, 41
- Patrício, V., Richard, J., Carton, D., et al. 2018, *MNRAS*, **477**, 18
- Petric, A. O., & Rupen, M. P. 2007, *AJ*, **134**, 1952
- Pillepich, A., Nelson, D., Springel, V., et al. 2019, arXiv:1902.05553
- Price, S. H., Kriek, M., Barro, G., et al. 2019, arXiv:1902.09554
- Price, S. H., Kriek, M., Shapley, A. E., et al. 2016, *ApJ*, **819**, 80
- Rathaus, B., & Sternberg, A. 2016, *MNRAS*, **458**, 3168
- Rix, H.-W., & Bovy, J. 2013, *A&ARv*, **21**, 61
- Romeo, A. B., & Agertz, O. 2014, *MNRAS*, **442**, 1230
- Romeo, A. B., & Falstad, N. 2013, *MNRAS*, **433**, 1389
- Saintonge, A., Lutz, D., Genzel, R., et al. 2013, *ApJ*, **778**, 2
- Sharples, R., Bender, R., Agudo Berbel, A., et al. 2013, *Msngr*, **151**, 21
- Sharples, R. M., Bender, R., Lehnert, M. D., et al. 2004, *Proc. SPIE*, **5492**, 1179
- Shetty, R., & Ostriker, E. C. 2012, *ApJ*, **754**, 2
- Shields, G. A. 1990, *ARA&A*, **28**, 525
- Silk, J. 2001, *MNRAS*, **324**, 313
- Simons, R. C., Kassin, S. A., Trump, J. R., et al. 2016, *ApJ*, **830**, 14
- Simons, R. C., Kassin, S. A., Weiner, B. J., et al. 2017, *ApJ*, **843**, 46
- Skelton, R. E., Whitaker, K. E., Momcheva, I. G., et al. 2014, *ApJS*, **214**, 24
- Stone, J. M., Ostriker, E. C., & Gammie, C. F. 1998, *ApJL*, **508**, L99
- Stott, J. P., Swinbank, A. M., Johnson, H. L., et al. 2016, *MNRAS*, **457**, 1888
- Sun, J., Leroy, A. K., Schrubba, A., et al. 2018, *ApJ*, **860**, 172
- Swinbank, A. M., Harrison, C. M., Trayford, J., et al. 2017, *MNRAS*, **467**, 3140
- Swinbank, A. M., Papadopoulos, P. P., Cox, P., et al. 2011, *ApJ*, **742**, 11
- Swinbank, A. M., Smail, I., Sobral, D., et al. 2012a, *ApJ*, **760**, 130
- Swinbank, A. M., Sobral, D., Smail, I., et al. 2012b, *MNRAS*, **426**, 935
- Tacchella, S., Carollo, C. M., Renzini, A., et al. 2015a, *Sci*, **348**, 314
- Tacchella, S., Lang, P., Carollo, C. M., et al. 2015b, *ApJ*, **802**, 101
- Tacconi, L. J., Genzel, R., Saintonge, A., et al. 2018, *ApJ*, **853**, 179
- Tacconi, L. J., Neri, R., Genzel, R., et al. 2013, *ApJ*, **768**, 74
- Tadaki, K., Iono, D., Yun, M. S., et al. 2018, *Natur*, **560**, 613
- Tamburro, D., Rix, H. W., Leroy, A. K., et al. 2009, *AJ*, **137**, 4424
- Toomre, A. 1964, *ApJ*, **139**, 1217
- Tully, R. B., & Fisher, J. R. 1977, *A&A*, **54**, 661
- Turner, O. J., Cirasuolo, M., Harrison, C. M., et al. 2017, *MNRAS*, **471**, 1280
- Übler, H., Förster Schreiber, N. M., Genzel, R., et al. 2017, *ApJ*, **842**, 121
- Übler, H., Genzel, R., Tacconi, L. J., et al. 2018, *ApJL*, **854**, L24
- Utomo, D., Blitz, L., & Falgarone, E. 2019, *ApJ*, **871**, 17
- van der Kruit, P. C., & Freeman, K. C. 1984, *ApJ*, **278**, 81
- van der Kruit, P. C., & Freeman, K. C. 2011, *ARA&A*, **49**, 301
- van der Wel, A., Bell, E. F., Häußler, B., et al. 2012, *ApJS*, **203**, 24
- van der Wel, A., Chang, Y.-Y., Bell, E. F., et al. 2014a, *ApJL*, **792**, L6
- van der Wel, A., Franx, M., van Dokkum, P. G., et al. 2014b, *ApJ*, **788**, 28
- Varidel, M., Pracy, M., Croom, S., Owers, M. S., & Sadler, E. 2016, *PASA*, **33**, e006
- Varidel, M. R., Croom, S. M., Lewis, G. F., et al. 2019, *MNRAS*, **485**, 4024
- Walter, F., Brinks, E., de Blok, W. J. G., et al. 2008, *AJ*, **136**, 2563
- Wang, B., & Silk, J. 1994, *ApJ*, **427**, 759
- Wang, H.-H., Klessen, R. S., Dullemond, C. P., van den Bosch, F. C., & Fuchs, B. 2010, *MNRAS*, **407**, 705
- Weiner, B. J., Willmer, C. N. A., Faber, S. M., et al. 2006, *ApJ*, **653**, 1027
- Whitaker, K. E., Franx, M., Leja, J., et al. 2014, *ApJ*, **795**, 104
- White, H. A., Fisher, D. B., Murray, N., et al. 2017, *ApJ*, **846**, 35
- Wilson, C. D., Warren, B. E., Irwin, J., et al. 2011, *MNRAS*, **410**, 1409
- Wisnioski, E., Förster Schreiber, N. M., Wuyts, S., et al. 2015, *ApJ*, **799**, 209
- Wisnioski, E., Glazebrook, K., Blake, C., et al. 2011, *MNRAS*, **417**, 2601
- Wisnioski, E., Glazebrook, K., Blake, C., et al. 2012, *MNRAS*, **422**, 3339
- Wisnioski, E., Mendel, J. T., Förster Schreiber, N. M., et al. 2018, *ApJ*, **855**, 97
- Wong, T., Hughes, A., Fukui, Y., et al. 2009, *ApJ*, **696**, 370
- Wuyts, S., Förster Schreiber, N. M., Genzel, R., et al. 2012, *ApJ*, **753**, 114
- Wuyts, S., Förster Schreiber, N. M., Lutz, D., et al. 2011, *ApJ*, **738**, 106
- Wuyts, S., Förster Schreiber, N. M., Wisnioski, E., et al. 2016, *ApJ*, **831**, 149
- Yoachim, P., & Dalcanton, J. J. 2006, *AJ*, **131**, 226
- Zhou, L., Federrath, C., Yuan, T., et al. 2017, *MNRAS*, **470**, 4573